Aalto University

Tuohino, Sasu; Vadimov, Vasilii; Teixeira, Wallace; Malmelin, Tommi; Silveri, Matti; Möttönen, Mikko

Multimode physics of the unimon circuit

Multimode physics of the unimon circuit

Sasu Tuohino [1,2,*], Vasilii Vadimov [1], Wallace Teixeira,[1] Tommi Malmelin [1], Matti Silveri [2], and Mikko Möttönen [1,3]

[1]*QCD Labs, QTF Centre of Excellence, Department of Applied Physics, Aalto University, P.O. Box 15100, FI-00076 Aalto, Finland*
[2]*Nano and Molecular Systems Research Unit, University of Oulu, P.O. Box 3000, FI-90014 Oulu, Finland*
[3]*VTT Technical Research Centre of Finland Ltd., QTF Center of Excellence, P.O. Box 1000, FI-02044 VTT, Finland*

We consider a superconducting half-wavelength resonator that is grounded at its both ends and contains a single Josephson junction. Previously this circuit was considered as a unimon qubit in the single-mode approximation where dc-phase-biasing the junction to π leads to increased anharmonicity and 99.9% experimentally observed single-qubit gate fidelity. Inspired by the promising first experimental results, we develop here a theoretical and numerical model for the detailed understanding of the multimode physics of the unimon circuit. To this end, first, we consider the high-frequency modes of the unimon circuit and find that even though these modes are at their ground state, they imply a significant renormalization to the Josephson energy. We introduce an efficient method to fully account for the relevant modes and show that unexcited high-lying modes lead to corrections in the qubit energy and anharmonicity. Interestingly, provided that the junction is offset from the middle of the circuit, we find strong cross-Kerr coupling strengths between a few low-lying modes. This observation paves the way for the utilization of the multimode structure, for example, as several qubits embedded into a single unimon circuit.

I. INTRODUCTION

Superconducting circuits are one of the most promising platforms to enable fault-tolerant quantum computing [1]. However, reaching the stage where such devices become useful in practical applications still seems a major challenge, calling for gate fidelities and coherence times beyond the current state-of-the-art qubits, such as transmons [2–4]. Even to achieve useful quantum advantage in the on-going noisy-intermediate-scale-quantum (NISQ) era [5], gate fidelities exceeding 99.99% for both single-qubit and two-qubit gates may be required, which has not been achieved in superconducting circuits yet. Thus, increasing the quality of superconducting qubits through design and fabrication is one of the greatest on-going technical challenges in the field.

Recently, different types of unconventional qubits combining desired features have been proposed as alternatives to transmons [6–26]. One of them, the fluxonium, has demonstrated coherence times of the order of milliseconds [10], and averaged gate fidelities exceeding 99.99% for single-qubit gates [10] and 99.7% for two-qubit gates [8,11], thus providing alternative routes towards large-scale quantum computers. However, the involved architecture of the fluxonium may limit its reproducibility in fabrication. In addition, its low frequency requires special techniques for control, readout, and reset [9].

The unimon is another unconventional qubit recently proposed and tested experimentally [27]. The unimon circuit exhibits simplicity since it consists of an inductively shunted single Josephson junction that can be biased by external flux. In contrast to the fluxonium, the unimon operates in the regime where the inductive energy of the shunt is mostly canceled by the quadratic component of the Josephson potential. Consequently, the unimon circuit promotes not only high anharmonicity but also full insensitivity to dc charge noise and reduced sensitivity to homogeneous flux noise. In particular, a comprehensive grasp of the fundamental multimode effects originating from the coupling between the Josephson junction and the coplanar waveguide (CPW) resonator is important. This is because the high-frequency modes of the CPW resonator can significantly alter the energy levels that encode the unimon qubit. The theoretical models employed in the description of the unimon to date have been restricted to the first and second-lowest normal modes of the system [27]. Even though they provide a good qualitative agreement with the experimental results, these models do not fully capture the influence of the high-frequency modes. Hence, there is a demand in development of more involved models of the unimon.

In this paper, we develop the theory of multimode unimon circuits and address the physical phenomena induced by its high-frequency modes. Starting from the continuous distributed-element circuit, we quantize the system obtaining an auxiliary-mode Hamiltonian that is equivalent to the effective Hamiltonian obtained using the path-integral-based approach in Ref. [27]. We then proceed with a partial linearization procedure [29–34] and find a renormalization of the Josephson energy [34,35] that was overlooked in Ref. [27]. The Hamiltonian is then represented in a unimon basis that allows for efficient numerical diagonalization within
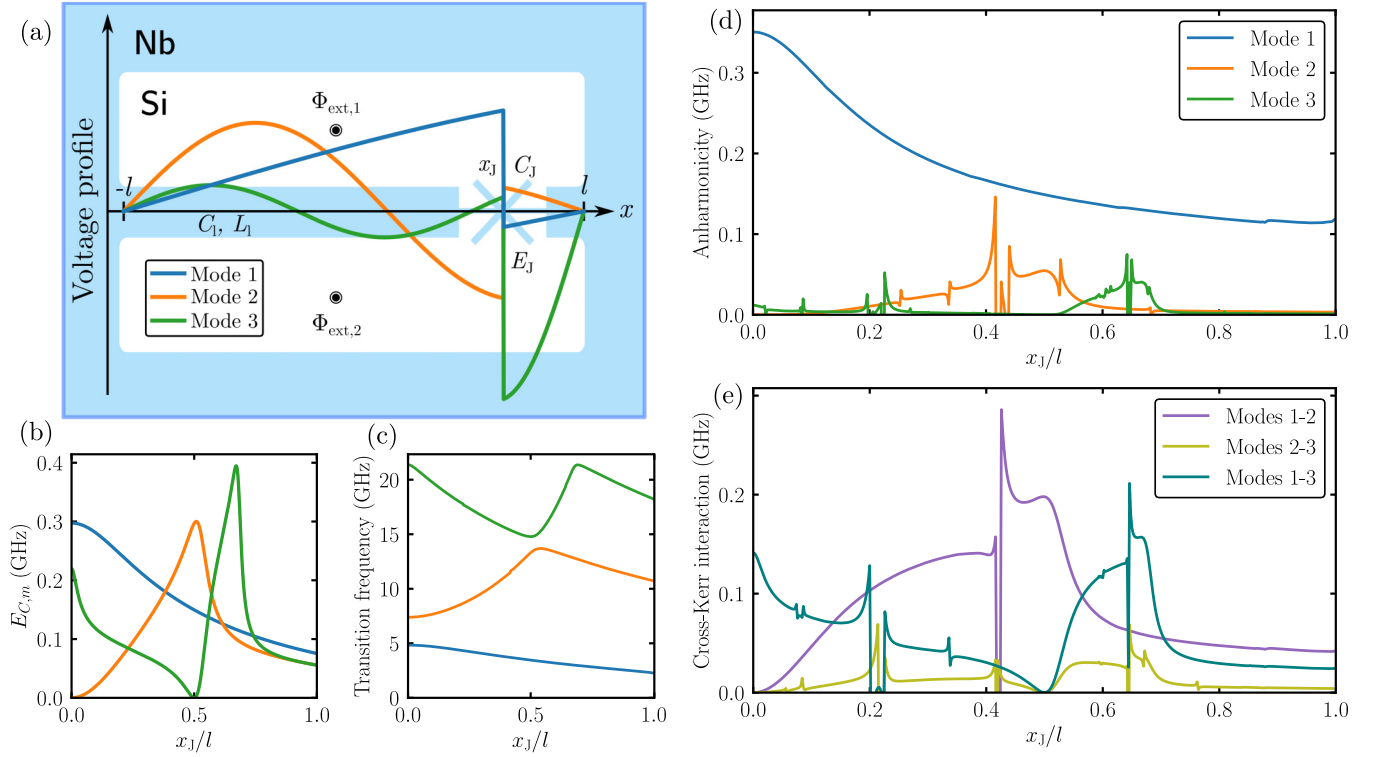
FIG. 1. (a) Schematic representation of a unimon circuit featuring a single Josephson junction (E_J, C_J) that is displaced from the center of the coplanar waveguide (CPW) resonator ($x_J \neq 0$) with a total length of $2l$. The CPW capacitance and inductance per unit length are denoted as C_l and L_l. The white regions symbolize silicon (Si), and the light blue areas represent niobium (Nb), excluding the Josephson junction composed of aluminum. The external magnetic flux biases through the first and second loops are labeled as $\Phi_{ext,1}$ and $\Phi_{ext,2}$. Voltage profiles for the first three modes ($m = 1, 2, 3$) are illustrated with solid lines [28]. The displacement of the Josephson junction renders its coupling to all modes to be more evenly distributed, as emphasized by the discontinuity in the voltage profile. Please note that the color-coding for the modes remains constant throughout the figure. (b) The effective charging energy $E_{C,m} = c_m^2 e^2/(2C_{eff})$, (c) transition frequency $(E_{m,1} - E_{m,0})/h$ of mode m, (d) anharmonicity [see Eq. (17)] of mode m, and (e) cross-Kerr interaction [see Eq. (18)] between modes $m - n$ as functions of the displacement x_J of the Josephson junction. For panels (b)–(e), the simulations were conducted using the parameter values from Table II with the number of low-lying modes set at $M_0 = 8$. The results depicted in (c)–(e) are derived from the energy levels featured in Fig. 3(a). As a consequence, the avoided crossings lead to visible discontinuities in these results.

the low-energy subspace, an approach that bears resemblance to the one introduced in Ref. [36]. We put forward an efficient method to obtain corrections of the qubit energies and anharmonicities induced by the coupling of the qubit mode to a several unoccupied high-frequency modes. For typical unimon parameters, we find anharmonicity reductions of roughly 30% when up to eight modes are taken into account.

Previously, unimon has been studied in the special case where junction is located at the center of the circuit, leading to half of the modes being decoupled from the junction. Importantly, our results indicate that an asymmetric arrangement where the junction is offset from the center provides a rich profile of distributed nonlinearity, which is expressed by significant self- and cross-Kerr couplings between the modes. Particularly, the numerical findings from both two- and three-mode scenarios display moderate nonlinearity across all modes concurrently, hinting at the potential for multimon-like qubit operations [37–39] within unimon circuits. However, to achieve high-fidelity multiqubit operations, unimon circuits with more intricate designs or additional components are likely needed. We further study the accuracy of our numerical findings by analytically solving for self- and cross-Kerr interactions within the harmonic-oscillator basis.

This paper is organized as follows. In Sec. II, we introduce our model and notation, detailing the linearization procedure and obtaining spectrum of the qubit. In Sec. III, we describe the effects of the high-frequency modes on the unimon-qubit mode comparing them with the results predicted by the single-mode model and the auxiliary-mode model introduced in Ref. [27]. In Sec. IV, we study the multimode structure of the unimon, focusing on the self- and cross-Kerr terms. Our conclusions are presented in Sec. V.

II. MULTIMODE MODEL FOR THE UNIMON

We study a single-junction unimon circuit with multiple modes taken into account. The system is schematically illustrated in Fig. 1(a). Our primary motivation is to understand how the position of the Josephson junction within the half-wavelength resonator influences the nonlinearity of the modes. Key indicators of this nonlinearity, namely the mode effective charging energy, transition frequency, anharmonicity, and cross-Kerr coupling between modes, are presented in Figs. 1(b)–1(e). To accurately compute these values, we introduce an effective theoretical model, which is elaborated upon in the subsequent sections. Table I provides

TABLE I. Descriptions for various symbols.

Symbol	Description
C_l	Capacitance per unit lenght of the CPW resonator
L_l	Inductance per unit lenght of the CPW resonator
C_J	Capacitance of the Josephson junction [40]
$2l$	Total lenght of the center conductor of the CPW resonator
x_J	Location of the Josephson junction on the center conductor of the CPW resonator; $x_J \in [-l, l]$
Φ_{diff}	Half difference of the applied external magnetic fluxes; $\Phi_{diff} = (\Phi_{ext,1} - \Phi_{ext,2})/2$
Φ_0	Magnetic flux quantum
ϕ_0	dc flux across the Josephson junction [Eq. (B3)]
φ_0	dc phase across the junction; $\varphi_0 = 2\pi\phi_0/\Phi_0$
Z_c	Characteristic impedance of the CPW resonator; $Z_c = \sqrt{L_l/C_l}$
M	The amount of auxiliary modes included into the auxiliary-mode Hamiltonian [Eq. (1)]
Ω_m	Resonance frequency of the m:th auxiliary mode, i.e., $\Omega_m = \pi m v/(2l)$. Corresponds to normal modes of the CPW resonator
C_{eff}	Effective capacitance felt by the flux across the Josephson junction [Eq. (2)]. Incorporates a correction originating from the CPW structure that vanishes as $M \to \infty$, i.e., $C_{eff} \to C_J$
L_{eff}	Effective inductance felt by the flux across the Josephson junction [Eq. (3)]. Incorporates an inductive shunt caused by the CPW resonator and an M dependent correction
ξ_m	Inductive coupling strength between the nonlinear mode and auxiliary mode [Eq. (4)]
M_0	The amount of *lower modes*, i.e., all unimon modes that include at least two energy levels with lower energy than E_{cutoff}
$\tilde{E}_J$ (E_J^*)	Renormalized Josephson energy in unimon (harmonic oscillator) basis [Eqs. (12) and (D1)]
$\tilde{L}_m$	Effective inductance of the m:th normal mode [Eq. (7)]
ω_m	Resonance frequency of the m:th normal mode
c_m	Contribution of m:th normal mode to flux across the Josephson junction [Eq. (5)]
$E_{C,m}$	Effective charging energy of the m:th normal mode; $E_{C,m}(\varphi_0) = c_m^2(\varphi_0)e^2/(2C_{eff})$
$E_{L,m}$	Effective inductive energy of the m:th normal mode; $E_{L,m}(\varphi_0) = \Phi_0^2/(2\pi)^2/[\tilde{L}_m c_m^2(\varphi_0)]$
λ_m	Zero-point fluctuations of m:th normal mode
α_m	Anharmonicity of m:th mode
K_{nm}	Cross-Kerr interaction between modes n and m

a compiled list of symbols used in the text, along with their descriptions.

A. Effective multimode unimon Hamiltonian

As a starting point for our multimode treatment of the unimon circuit, we use a Hamiltonian that comprises a nonlinear mode with $\hat{\Psi}$ describing the magnetic flux

difference across the Josephson junction and being conjugate to the charge $\hat{Q}$. In addition, the Hamiltonian includes M linear auxiliary modes with fluxes $\hat{\chi}_m$ that are conjugate to charges $\hat{\Xi}_m$, where $m = 1, \ldots, M$. The relevant nonzero single-operator commutation relations these operators satisfy are $[\hat{\Psi}, \hat{Q}] = i\hbar$ and $[\hat{\chi}_k, \hat{\Xi}_m] = i\hbar\delta_{km}$. A detailed derivation for the Hamiltonian is provided in the Appendix A, and hence, we begin our treatment from the auxiliary-mode Hamiltonian

$$
\begin{aligned}
\hat{H}_{aux} = {} & \frac{\hat{Q}^2}{2C_{eff}} + \frac{\hat{\Psi}^2}{2L_{eff}} + \frac{\hat{\Psi}}{2lL_l}(\Phi_{diff} - \phi_0) \\
& - E_J \cos\left[\frac{2\pi}{\Phi_0}(\hat{\Psi} - \phi_0)\right] \\
& + \sum_{m=1}^{M}\left[\frac{\hat{\Xi}_m^2}{2C_{eff}} + \frac{1}{2}C_{eff}\Omega_m^2\hat{\chi}_m^2 + \xi_m\hat{\chi}_m\hat{\Psi}\right], \quad (1)
\end{aligned}
$$

where C_{eff} and L_{eff} are the effective lumped capacitance and inductance of the nonlinear mode, $2l$ is the resonator length, $\Phi_{diff} = (\Phi_{ext,1} - \Phi_{ext,2})/2$ is the half difference of the external magnetic fluxes shown in Fig. 1(a), ϕ_0 is the dc magnetic flux offset across the Josephson junction (Appendix A), E_J is the Josephson energy, Φ_0 denotes the flux quantum, $\Omega_m = \pi m v/(2l)$ is the resonance angular frequency of the auxiliary mode m, and $\{\xi_m\}$ are the coupling strengths of the auxiliary modes to the nonlinear mode. The definitions for the effective lumped-element capacitance and inductance are

$$
C_{eff} = C_J + \frac{C_l(l^2 + 3x_J^2)}{6l} - \sum_{m=1}^{M}\frac{\cos^2\left(\frac{\Omega_m x_J}{v} + \frac{m\pi}{2}\right)}{\Omega_m^2 lL_l}, \quad (2)
$$

$$
L_{eff} = 2lL_l\left[1 + \sum_{m=1}^{M}2\cos^2\left(\frac{\Omega_m x_J}{v} + \frac{m\pi}{2}\right)\right]^{-1}, \quad (3)
$$

and the auxiliary-mode coupling strengths are

$$
\xi_m = \sqrt{\frac{C_{eff}}{lL_l}}\Omega_m\cos\left(\frac{\Omega_m x_J}{v} + \frac{m\pi}{2}\right), \quad (4)
$$

where $v = 1/\sqrt{L_lC_l}$ is the phase velocity, C_J is the capacitance of the Josephson junction [40], C_l denotes the capacitance per unit length, and $x_J \in [-l, l]$ represents the location of the Josephson junction in the CPW resonator.

Intuitively, the auxiliary-mode Hamiltonian can be thought of as a nonlinear oscillator (first two rows) that is linearly coupled (last term) with a set of linear oscillators (first two terms on the last row) referred to as auxiliary modes. From a physical perspective, the nonlinear oscillator corresponds to the flux difference across the Josephson junction, whereas the auxiliary modes can be thought of as the normal modes of the CPW resonator in the absence of the Josephson junction.

The auxiliary-mode Hamiltonian in Eq. (1) contains M auxiliary modes. Although this expression becomes exact as $M \to \infty$, numerical calculations necessitate limiting the number of modes at a finite M. Note that even when we set $M = 0$, the nonlinear oscillator feels the effect of the CPW modes through the inductive shunt and capacitive correction given by the first term in Eq. (3) and second term in Eq. (2). How to choose M is addressed in more detail in Sec. III.

The auxiliary modes couple to the nonlinear mode inductively, providing corrections to the unimon qubit energy levels. The auxiliary-mode Hamiltonian in Eq. (1) is well-adapted for studying the unimon circuit if our interest is focused only on the lowest mode, as in Ref. [27]. Since the auxiliary-mode frequencies are integer multiples of the lowest auxiliary mode, $\Omega_m = \pi m v/(2l)$, only the few lowest modes are energetically close enough to the nonlinear mode $\hat{\Psi}$ to significantly interact with it. Furthermore, the location of the Josephson junction can be chosen strategically to leave certain auxiliary modes uncoupled, thus reducing the computational load. In an optimal scenario, this approach allows for fairly accurate results for unimon qubit energy levels to be obtained by incorporating just a single auxiliary mode, effectively reducing the problem to solving a two-dimensional Schrödinger equation in the flux basis [27]. However, extending the consideration from the energy levels of the lowest mode to those of a multimode system necessitates an alternative approach, primarily due to the rapid escalation of computational demand as more auxiliary modes are included.

To adapt the Hamiltonian of the unimon circuit for numerical analysis in cases involving multiple modes, we divide the auxiliary-mode Hamiltonian in Eq. (1) into linear and non-linear parts, $\hat{H}_{\text{aux}} = \hat{H}_{\text{lin}} + \hat{H}_{\text{nl}}$, by expanding the nonlinear Josephson term and moving the resulting quadratic term to the linear part (Appendix B). To elucidate different modes in the system and simplify subsequent analysis, we find the classical normal modes of the linear part, $\hat{H}_{\text{lin}}$, using a basis transformation. This process, which effectively removes the linear coupling between the flux operators in Eq. (1), is detailed in the Appendix B. We note that similar linearization procedures to find the normal modes of system have been employed in earlier works, as seen in Refs. [29–34]. The basis transformation gives rise to the normal-mode flux operators and the corresponding conjugate charge operators which are denoted by $\hat{\phi}_m$ and $\hat{q}_m$, respectively. These new operators continue to satisfy the canonical commutation relations $[\hat{\phi}_k, \hat{q}_m] = i\hbar \delta_{km}$. The transformation also yields the normal-mode representation of the magnetic flux across the Josephson junction:

$$\hat{\Psi} = \sum_{m=1}^{M+1} c_m \hat{\phi}_m, \tag{5}$$

where the constant factors c_m are coefficients determined by the transformation and describe the contribution from each normal mode to the overall magnetic flux across the junction. In addition, the diagonalization process reveals the normal-mode frequencies, denoted by $\omega_m/(2\pi)$, $m = 1, \ldots, M+1$. Insertion of Eq. (5) into the nonlinear part $\hat{H}_{\text{nl}}$ gives us the full normal-mode representation of the Hamiltonian in Eq. (1) as

$$\hat{H}_{\text{aux}} = \sum_{m=1}^{M+1} \left[\frac{\hat{q}_m^2}{2C_{\text{eff}}} + \frac{\hat{\phi}_m^2}{2\tilde{L}_m} + I_c \sin\left(\frac{2\pi\phi_0}{\Phi_0}\right) c_m \hat{\phi}_m \right]$$
$$- E_{\text{J}} \cos\left[\frac{2\pi}{\Phi_0} \left(\sum_{m=1}^{M+1} c_m \hat{\phi}_m - \phi_0 \right) \right]$$
$$- \frac{1}{2L_{\text{J}}} \cos\left(\frac{2\pi\phi_0}{\Phi_0}\right) \sum_{\substack{m,k=1 \\ m \neq k}}^{M+1} c_m c_k \hat{\phi}_m \hat{\phi}_k, \tag{6}$$

where we have defined the Josephson inductance $L_{\text{J}} = (\Phi_0/2\pi)^2/E_{\text{J}}$, the critical current $I_c = 2\pi E_{\text{J}}/\Phi_0$ and

$$\tilde{L}_m = \left[C_{\text{eff}}\omega_m^2 - \frac{\cos(2\pi\phi_0/\Phi_0)}{L_{\text{J}}} c_m^2 \right]^{-1}, \tag{7}$$

to represent the effective inductance of the m:th normal mode.

Above, we described the Hamiltonian of the unimon circuit in the normal-mode basis of the linearized version of the circuit. However, the challenge still remains, since finding the energy levels of the unimon qubit, while including the interactions from the higher number of modes, requires solving a high-dimensional Schrödinger equation. Thus an improved basis is needed.

To simplify the notation, we introduce dimensionless operators $\hat{n}_m = (\hat{q}_m/c_m)/(2e)$ and $\hat{\varphi}_m = 2\pi c_m \hat{\phi}_m/\Phi_0$, where e is the elementary charge. We divide the Hamiltonian in Eq. (6) into parts describing the single-mode unimon Hamiltonians $\hat{H}_m$ and the interaction part $\hat{H}_{\text{int}}$, leading to

$$\hat{H}_{\text{aux}} = \sum_{m=1}^{M+1} \hat{H}_m + \hat{H}_{\text{int}}. \tag{8}$$

These constituent Hamiltonians can be expressed as

$$\hat{H}_m = 4E_{C,m}(\varphi_0)\hat{n}_m^2 + \tfrac{1}{2}E_{L,m}(\varphi_0)\hat{\varphi}_m^2$$
$$+ E_{\text{J}}[\sin(\varphi_0)\hat{\varphi}_m - \cos(\hat{\varphi}_m - \varphi_0)] \tag{9}$$

and

$$\hat{H}_{\text{int}} = E_{\text{J}} \left[\sum_{m=1}^{M+1} \cos(\hat{\varphi}_m - \varphi_0) - \cos\left(\sum_{m=1}^{M+1} \hat{\varphi}_m - \varphi_0 \right) \right.$$
$$\left. - \frac{\cos(\varphi_0)}{2} \sum_{\substack{m,k=1 \\ m \neq k}}^{M+1} \hat{\varphi}_m \hat{\varphi}_k \right], \tag{10}$$

where we have defined an effective charging energy of the m:th mode as $E_{C,m}(\varphi_0) = c_m^2(\varphi_0)e^2/(2C_{\text{eff}})$, effective inductive energy as $E_{L,m}(\varphi_0) = \Phi_0^2/(2\pi)^2/[\tilde{L}_m c_m^2(\varphi_0)]$, and the dc phase across the junction is denoted as $\varphi_0 = 2\pi\phi_0/\Phi_0$. Note that the coefficients c_m introduce the dependence of $E_{C,m}$ and $E_{L,m}$ on φ_0.

This normal-mode representation of the auxiliary-mode Hamiltonian is beneficial for several reasons. On one hand, it fully separates the single-mode components from the interaction terms. This becomes particularly clear on the first row of Eq. (10), where the first term cancels the concealed single-mode terms in the second term (see Appendix C). Due to the utilization of normal mode coordinates of $\hat{H}_{\text{lin}}$, the interaction part $\hat{H}_{\text{int}}$ is exclusively composed of nonlinear interactions. On the other hand, the single-mode unimon Hamiltonian $\hat{H}_m$ can be diagonalized efficiently using the one-dimensional Schrödinger equation, $\hat{H}_m|j_m\rangle = E_{m,j}|j_m\rangle$, where $|j_m\rangle$ and $E_{m,j}$ denote the j:th eigenstate of the m:th mode and the corresponding eigenenergy. In the remaining text, the energy levels are assumed to be shifted such that $E_{m,0} = 0$. Moreover, the eigenstates of $\hat{H}_m$ form a set of basis states (referred as *unimon basis*) that can be used to represent the interaction part $\hat{H}_{\text{int}}$ in a matrix form. In practice, this is accomplished by applying the generalized trigonometric sum

relation

$$\cos\left(\sum_{i=1}^{N}\hat{\varphi}_i\right) = \sum_{\substack{k=0 \\ \text{even } k}}^{N}(-1)^{\frac{k}{2}}\sum_{\substack{A\subseteq\{1,\ldots,N\} \\ |A|=k}}$$

$$\times\left[\prod_{i\in A}\sin(\hat{\varphi}_i)\prod_{i\notin A}\cos(\hat{\varphi}_i)\right] \quad (11)$$

for a cosine of sums, and subsequently calculating matrix elements of three different types, $\langle j_m|\cos(\hat{\varphi}_m)|j'_m\rangle$, $\langle j_m|\sin(\hat{\varphi}_m)|j'_m\rangle$, and $\langle j_m|\hat{\varphi}_m|j'_m\rangle$, in Eq. (10). The last summation in Eq. (11) represents a sum over all possible subsets of $\{1,\ldots,N\}$ with a size of k. The product over $i\notin A$ refers to all elements in $\{1,\ldots,N\}$ not included in A. When $k=0$, A is an empty set, and the product over $i\notin A$ encompasses all elements of $\{1,\ldots,N\}$.

The form of the single-mode unimon Hamiltonian in Eq. (9) is equivalent with the model 1 introduced in Ref. [27]. Intuitively, it can be interpreted as a nonlinear oscillator composed of a Josephson junction with effective inductive and capacitive shunts. Both of these shunts, as well as the nonlinear Josephson junction term, depend on the external magnetic field. While these effective shunts and their dependence on the external magnetic field physically originate from the CPW resonator structure, the single-mode approach falls short in accurately capturing the multimode effects. This is the point at which the interaction Hamiltonian in Eq. (10) becomes significant and our model effectively diverges from the single-mode approach presented in Ref. [27].

B. Energy cutoff for Hilbert space

After establishing a matrix representation in the unimon basis, we need to manage the dimensions of the Hilbert space before proceeding with an efficient diagonalization of the matrix. To this end, we restrict the total size of the Hilbert space, which ensures computational feasibility and accuracy of the numerical approximations.

Although the number of energy levels for each mode is theoretically infinite, ideal quantum computation takes place in a finite-dimensional space and, therefore, is compatible with the concept of an energy cutoff, E_{cutoff}. Consequently, we disregard all eigenstates of the single-mode unimon Hamiltonian $\hat{H}_m$ with energies exceeding E_{cutoff}. The value of the energy cutoff is determined by the convergence of the low-energy eigenstates of the full Hamiltonian that we aim to

accurately model. Since the bare frequencies of the modes increase with the mode number m, we only need to consider states beyond the ground state for a limited number of modes. This is attributed to the fact that the energy required to excite such a mode exceeds the established energy cutoff. Although eigenstates with energy below the cutoff can interact with those above it, the significance of these interactions (including higher-order processes) diminishes as E_{cutoff} is increased. This effect is particularly pronounced for low-energy eigenstates, which have the potential to be utilized for encoding qubits. The convergence of low-energy eigenstates with respect to the energy cutoff is briefly addressed in Appendix E.

We categorize the complete set of modes ($m = 1, 2, \ldots, M+1$) into two distinct groups, referred to as the *lower modes* and *higher modes*. The lower modes, defined by an integer M_0 and $m \in \{1, \ldots, M_0\}$, include all modes where any excited states are considered. Conversely, for the higher modes, for which $m \in \{M_0+1, \ldots, M+1\}$, only their vacuum state is included due to the energy cutoff.

To simplify numerical computations, we assume that the system is operated at a flux sweet spot where $\Phi_{\text{diff}} = \Phi_0/2$ and $\varphi_0 = \pi$. This condition results in a symmetry $\langle\varphi_m|j_m\rangle = |\langle-\varphi_m|j_m\rangle|$. For the vacuum state, we have $\langle\varphi_m|0_m\rangle = \langle-\varphi_m|0_m\rangle$, and hence the expectation values of operators antisymmetric in $\hat{\varphi}_m$ vanish for the vacuum sate. For example, $\langle 0_m|\sin(\hat{\varphi}_m)|0_m\rangle = 0$ and $\langle 0_m|\hat{\varphi}_m|0_m\rangle = 0$. Interestingly, utilization of the energy cutoff and symmetric eigenstates implies that the impact of the higher modes on the system primarily contributes to a renormalization of the Josephson energy, denoted as

$$\tilde{E}_{\text{J}} = E_{\text{J}}\prod_{m=M_0+1}^{M+1}\langle 0_m|\cos(\hat{\varphi}_m)|0_m\rangle. \quad (12)$$

The physical origin of this effect is in the zero-point fluctuations of the higher modes that interact with the lower modes through the second term in Eq. (10). A more comprehensive exploration of this renormalization effect and its implications can be found in Sec. III.

After incorporating all of the above-described steps, we arrive at the final form of the total Hamiltonian

$$\hat{H}_{\widetilde{\text{aux}}} = \sum_{m=1}^{M_0}\hat{H}_m + \hat{H}_{\widetilde{\text{int}}}, \quad (13)$$

where the Hilbert space has been truncated based on the energy cutoff, and the interaction term is expressed as

$$\hat{H}_{\widetilde{\text{int}}} = -E_{\text{J}}\left[\sum_{n=1}^{M_0}\cos(\hat{\varphi}_n) - \frac{1}{2}\sum_{\substack{l,k=1 \\ l\neq k}}^{M_0}\hat{\varphi}_l\hat{\varphi}_k\right] + \sum_{\substack{j=0 \\ \text{even } j}}^{M_0}(-1)^{\frac{j}{2}}\sum_{\substack{A\subseteq\{1,\ldots,M_0\} \\ |A|=j}}\tilde{E}_{\text{J}}\left[\prod_{i\in A}\sin(\hat{\varphi}_i)\prod_{i\notin A}\cos(\hat{\varphi}_i)\right], \quad (14)$$

after using Eq. (11). We consider this form of the total Hamiltonian to be one of the main results of this paper.

In our model, the Hamiltonian described by Eq. (13) is expressed in a matrix form using the unimon basis, where

matrix elements are expressed as

$$[H_{\widetilde{\text{aux}}}]_{i_0 j_1\ldots k_{M_0}}^{i'_0 j'_1\ldots k'_{M_0}} = \langle i_0 j_1\ldots k_{M_0}|\hat{H}_{\widetilde{\text{aux}}}|i'_0 j'_1\ldots k'_{M_0}\rangle, \quad (15)$$
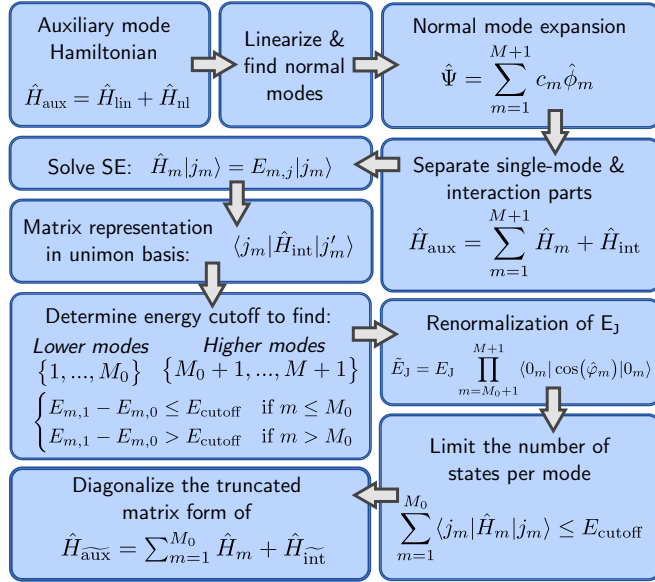
FIG. 2. Process chart illustrating the method for solving the energy levels and eigenstates of the unimon circuit in a multimode scenario. This schematic provides a visual summary of the more detailed instructions and definitions given in Sec. II.

FIG. 3. Energy levels of the unimon circuit as functions of (a) the location of the Josephson junction x_J, (b) Josephson energy E_J, and (c) characteristic impedance Z_c of the CPW. The solid lines represent the qubit subspace of the three first modes, under the condition that the rest of the modes are in their vacuum state. All other states are represented by dashed lines. The inset of panel (a) provides a close view of an example avoided crossing. For these simulations, we used the parameters from Table II, with the number of lower modes set to $M_0 = 8$. Note that the sweep of the characteristic impedance is carried out in such a way that the frequency of the lowest auxiliary mode, represented by $\Omega_1 = \pi/(2l\sqrt{L_lC_l})$, remains constant.

and each state $|i_0 j_1 \ldots k_{M_0}\rangle$ must meet the energy cutoff condition

$$\left\langle i_0 j_1 \ldots k_{M_0} \left| \sum_{m=1}^{M_0} \hat{H}_m \right| i_0 j_1 \ldots k_{M_0} \right\rangle \leqslant E_{\text{cutoff}}. \quad (16)$$

By carefully selecting the energy cutoff, the diagonalization of the matrix can be accomplished with adequate numerical efficiency and accuracy.

The above-introduced process of solving the eigenstates of the unimon circuit is visually summarized in Fig. 2.

C. Labeling of eigenstates

Upon diagonalizing the matrix, we acquire a new set of eigenstates along with corresponding energy eigenvalues, which can be interpreted as perturbed versions of the single-mode Hamiltonian [Eq. (9)] eigenstates. To enhance our understanding of the effects of the interactions between the modes, it is fruitful to study the energy differences between the perturbed and noninteracting scenarios.

Although visual inspection of the energy levels can yield insight in specific cases, this approach tends to become increasingly demanding in general. To streamline this process, we compare the energy eigenstates of the interacting Hamiltonian with those of the noninteracting case. In practice, this is achieved by calculating the state overlaps $|\langle i_0 j_1 \ldots k_{M_0}|\alpha_n\rangle|$, where $|\alpha_n\rangle$ represents the n:th eigenstate of $\hat{H}_{\widetilde{\text{aux}}}$ and $|i_0 j_1 \ldots k_{M_0}\rangle$ corresponds to an eigenstate of the noninteracting Hamiltonian $\sum_{m=1}^{M_0} \hat{H}_m$. We then identify the state $|i_0 j_1 \ldots k_{M_0}\rangle$ that exhibits the maximum overlap with $|\alpha_n\rangle$, and label $|\alpha_n\rangle$ as the perturbed counterpart of $|i_0 j_1 \ldots k_{M_0}\rangle$.

Note that our labeling method may produce ambiguous results. This ambiguity arises from transverse-type interactions introduced by the interaction term, leading to strong
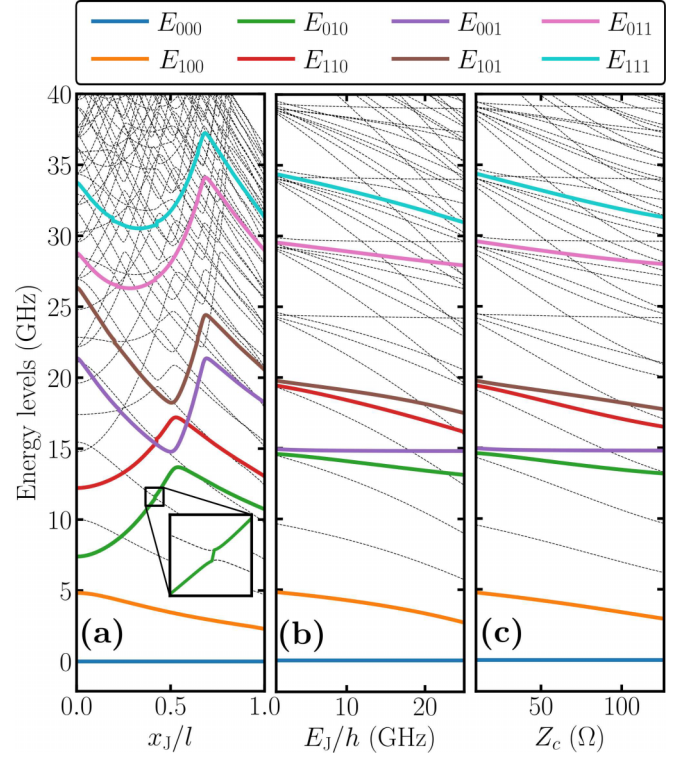
hybridization between eigenstates near suitable degeneracy points. Figure 3(a) illustrates the effects of the hybridization in the energy level diagram, exhibiting avoided crossings between levels. Where eigenstate labeling is applied on quantities such as anharmonicity or cross-Kerr interaction, the effects of hybridization are exposed through sudden discontinuities as found in Figs. 1(d) and 1(e).

D. Summary of different models for unimon

Here, we summarize the different unimon models that are relevant for the remaining text. We started with the auxiliary-mode Hamiltonian in flux basis [Eq. (1)]. While its derivation employs a different approach, this Hamiltonian is equivalent to the one derived using the path-integral-based model detailed in Ref. [27] (see Appendix A). The auxiliary-mode Hamiltonian becomes exact at the limit $M \rightarrow \infty$. However, realistically, it can only be solved for a limited number of auxiliary modes. We refer to this way of solving the eigenstates and their energies as *auxiliary-mode model* (AMM). We note that the presentation of the auxiliary-mode Hamiltonian in Eq. (1) differs slightly from the one presented in Ref. [27]. The distinction lies in the dc flux offset parameter ϕ_0 that

TABLE II. Physical parameters used in the simulations unless otherwise explicitly stated.

$2l$ (mm)	L_l (μH/m)	C_l (pF/m)	C_J (fF)	E_J/h (GHz)	x_J/l (-)	Z_c (Ω)	$\Omega_1/(2\pi)$ (GHz)	Φ_{diff}/Φ_0 (-)
8.0	0.821	87.1	1.4	19.0	0.51	97.1	7.39	0.5

we introduce (Appendix A) to facilitate our derivation of the multimode model.

In our treatment above, the auxiliary-mode Hamiltonian has been transformed into normal-mode coordinates and separated into single-mode and interaction components, as illustrated in Eq. (8). The single-mode components in Eq. (9) closely resemble the model 1 from Ref. [27], which also employs normal-mode coordinates. In fact, the two models become equivalent as $M \to \infty$. However, an excellent approximation is also achieved for a finite number of auxiliary modes (e.g., $M \approx 100$). We define this single-mode approach as the *single-mode model* (SMM). While this model is the simplest to solve, it compromises accuracy by neglecting the interaction component described in Eq. (10).

In Eq. (12), we define a renormalized version of the Josephson energy to approximate the influence of higher modes on the system. As a special case of this, we consider $M_0 = 1$, where all modes except the lowest one are categorized as higher modes. This assumption leads to a modified version of the single-mode Hamiltonian in Eq. (9), where the standard E_J is replaced with the renormalized $\tilde{E}_J$. We denote this as the *renormalized single-mode model* (RSSM). The advantage of this model is that it retains the simplicity and efficiency of the single-mode model, while enhances accuracy by incorporating the zero-point fluctuations of the higher modes.

The main result of our derivations is presented in Eq. (13). We obtained this Hamiltonian by imposing the energy cutoff condition in Eq. (16). In order to determine the eigenstates and corresponding energy levels, the Hamiltonian is diagonalized in the unimon basis. We refer to this approach as the *multimode model* (MMM). Its primary advantage lies in the improved accuracy through the inclusion of multimode interactions [Eq. (14)], while simultaneously maintaining efficiency by truncating the Hilbert space.

III. MULTIMODE EFFECTS IN THE UNIMON CIRCUIT

Our next step is to analyze how the modes above the lowest mode affect the energy levels and anharmonicity of the lowest mode. This is important since the lowest mode is typically used to encode a unimon qubit. First, we focus on the anharmonicity calculated by using the renormalized single-mode model, and compare it with the previously used single-mode model in Eq. (9). Second, we discuss the anharmonicity results from the multimode model [Eq. (13)] and juxtapose them with the outcomes of the renormalized single-mode model. As a further point of comparison, we discuss how the above-mentioned models compare with the auxiliary-mode model [Eq. (1)].

A. Effect of renormalization

As indicated in Eq. (12), the higher modes influence the energy levels of the unimon even in their vacuum state through zero-point phase fluctuations. These fluctuations couple to

the lowest mode, effectively causing a renormalization of the Josephson energy within the system [34,35]. Since the renormalization coefficient is simply a product of the vacuum state expectation values of a cosine function, it follows that $\tilde{E}_J/E_J \leqslant 1$. As a result, we observe a decrease in the anharmonicity of the lowest mode.

Interestingly, this decrease in anharmonicity due to the renormalization of the Josephson energy offers an explanation for the discrepancies observed between the single-mode model and the auxiliary-mode model used in Ref. [27]. The auxiliary-mode model, as described in Eq. (1), is expected to yield more accurate results when a few low-frequency linear modes are included compared to the single-mode model that incorporates only one normal mode.

In Fig. 4(a), the anharmonicities of the lowest mode, as calculated with each model, are displayed. Between the single-mode and auxiliary-mode ($M = 2$) models the difference is roughly 20% at $x_J = 0$. By including the renormalization (RSSM), we observe an approximate 20% decrease in the anharmonicity compared to the single-mode model, bringing the result close to the predictions of the auxiliary-mode model. In Fig. 4(b), we further detail the behavior of the renormalization coefficient, which changes only weakly as a function of x_J.

It is worth mentioning that based on physically motivated mode-cutoff frequencies [34,41], the number of modes M included in the renormalization process should be finite. Here we introduce a cutoff that is based on the magnitude of the superconductor gap parameter Δ_{gap}. Namely, we set $\Omega_m \leqslant 2\Delta_{gap}$, which imposes a limit on the number of modes [34,42,43]. However, the renormalization coefficient appears to be insensitive to the precise number of modes included and seems to converge as $M \to \infty$. This is demonstrated in the inset of Fig. 4(b), which shows that the contribution from each mode around the cutoff frequency ($M \approx 100$) is negligible. More detailed discussion regarding the convergence of the renormalization coefficient is found in Appendix D.

Our numerical findings shown in Fig. 4 demonstrate that the renormalization of the Josephson energy leads to anharmonicities close to those obtained from the flux basis solution of the auxiliary-mode Hamiltonian. Importantly, compared to the single-mode model, the renormalized single-mode model achieves a level of accuracy comparable to the auxiliary-mode approach ($M = 2$), with virtually no increase in the computational load.

B. Effects beyond renormalization

In addition to the renormalization effect of vacuum states, we aim to understand how the energy levels of the unimon qubit are influenced when some excited eigenstates in modes $m > 1$ are kept within the computational Hilbert space. Therefore we employ the multimode model to determine the energy levels and anharmonicities of the full Hamiltonian in the unimon basis as shown in Eq. (15). The truncation of the
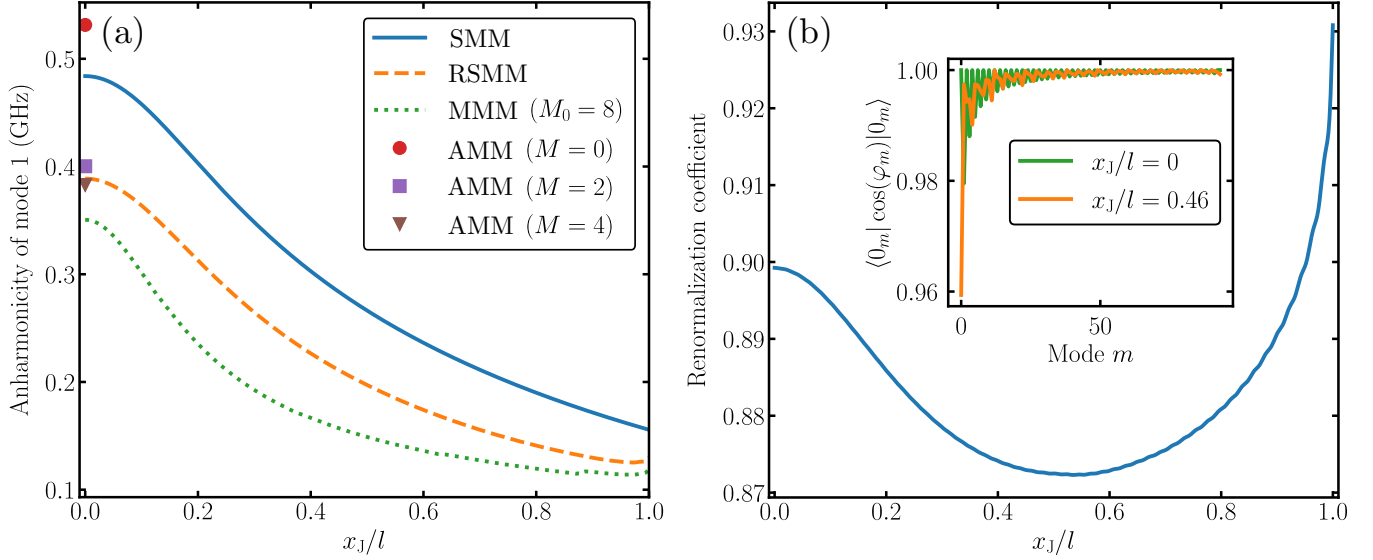
FIG. 4. (a) Anharmonicity of the unimon qubit encoded into the lowest-frequency mode and (b) the renormalization coefficient $\tilde{E}_J/E_J$ as function of the location of the junction x_J. We show in (a) the anharmonicity obtained using the single-mode model (solid line), renormalized single-mode model (dashed line), and the multimode model (dotted line) including $M_0 = 8$ lower modes. The anharmonicities computed directly from the auxiliary-mode model at $x_J = 0$ are indicated by markers, accounting for different numbers of auxiliary modes: $M = 0$ (circle), $M = 2$ (square), and $M = 4$ (triangle). The inset in (b) shows the contribution from each mode to the renormalization coefficient for $x_J/l = 0$ (green line) and $x_J/l = 0.46$ (orange line) [see Eq. (12)]. These numerical calculations are carried out using the parameters listed in Table II.

Hilbert space is executed based on an energy cutoff, which is set to be at least several times higher than the highest energy level utilized for qubit encoding. Our findings show that the anharmonicity is further reduced when compared to the renormalized single-mode model. This indicates that the multimode model should be used to achieve accurate results.

We also propose that this model exhibits higher numerical accuracy with a given number of computational resources compared to solving the auxiliary-mode model in the flux basis. This claim is supported by two factors. First, solving the auxiliary-mode model becomes in general very challenging for increasing $M > 2$ owing to the exponential increase in the dimension of the computational Hilbert space. Second, as depicted in Fig. 4, the results derived from the auxiliary-mode model appear to converge towards those obtained from our multimode model with increasing M. However, due to the substantial computational demand imposed by the auxiliary-mode model, we are unable to verify this comprehensively. Note that, in special cases such as $x_J/l = 0$, we are capable of solving the auxiliary-mode model for $M = 4$ since only auxiliary modes with an even ordinal number exhibit nonzero coupling with the nonlinear mode. In addition, we emphasize that the multimode model requires significantly less computational time than the auxiliary-mode model to achieve a comparable accuracy. More details on the accuracy of the multimode model can be found in Appendix E.

IV. INTERACTIONS BETWEEN THE LOWEST MODES OF THE UNIMON CIRCUIT

A. Energy levels and avoided crossings

Let us leverage the model developed in Sec. II to its full extent by examining the interactions among the three lowest

modes of the unimon circuit. This involves solving the multimode Hamiltonian in the unimon basis as given in Eqs. (15), and subsequently employing our labeling method to map the obtained eigenstates onto the states of the unimon basis. The energies of the labeled eigenstates are denoted as E_{ijk}, where i, j, and k represent the number of excitations in the first, second, and third modes, respectively. In Fig. 3, we show all obtained energy levels as functions of x_J, E_J, and Z_c. Here, $Z_c = \sqrt{L_l/C_l}$ represents the characteristic impedance of the transmission line forming the resonator. Within the energy levels, we highlight the labeled states where each of the initial three modes has at most one excitation. In Fig. 3(a), the energy levels manifest fairly intricate interactions with each other as a function of x_J. We observe a correlation between the first excited states and the effective charging energies shown in Fig. 1(b), which is evident in the alignment of the local extrema. The effective charging energy for the mode depends on the weight coefficient c_m which is related to the coupling between the Josephson junction and mode m [see Eq. (5)]. Figures 3(b) and 3(c) illustrate that an increase in either the Josephson energy or the characteristic impedance results in a decrease in energy for the first excited states. This behavior can be attributed to the cancellation of quadratic terms as either E_J or Z_c increases. As these quadratic terms decrease, the potential becomes less steep, which in turn narrows the energy gap between the ground state and the excited states. However, the energies of the excited states of the third mode remain largely unchanged, given their weak coupling with the Josephson junction. As discussed in Sec. II C, these interactions often manifest as avoided crossings. An interaction exemplifying this can be observed between energy levels E_{010} and E_{300} at $x_J/l = 0.42$, visualized in the inset of Fig. 3(a).

In qubit operations, avoided crossings are undesirable. If qubit energy levels become hybridized, there is a risk of unintended leakage into other participating states. This can adversely affect the coherence time of the qubit. Consequently, it is preferable to operate in parameter regimes where hybridization of the qubit states is minimized. The prevalence of avoided crossings increases with energy, rendering the use of high-frequency normal modes ($m \geqslant 2$) challenging for qubit operation. Nonetheless, in most parameter regimes, the qubit of the lowest mode ($m = 1$) remains unaffected by these avoided crossings up to its second excited state.

B. Anharmonicities and cross-Kerr interactions

We employ the labeled energy levels to compute key properties, such as the anharmonicity and cross-Kerr interaction. For the lowest mode $m = 1$, the anharmonicity is defined as

$$\alpha_1(i, k) = \frac{(E_{2ik} - E_{1ik}) - (E_{1ik} - E_{0ik})}{h}, \quad (17)$$

and the cross-Kerr interaction between the modes 1 and 2 is defined as

$$K_{12}(i) = \frac{(E_{11i} - E_{01i}) - (E_{10i} - E_{00i})}{h}. \quad (18)$$

In general, the subscripts in α_m and K_{mn} define which modes are considered. It is customary to consider anharmonicity involving only one mode and cross-Kerr interaction involving two modes. However, higher-order terms become significant when excitations in other modes are allowed. In this case, the anharmonicity of a mode depends on the occupation number of the other two modes, while the cross-Kerr interaction between two given modes is influenced by the state of the third mode. We consider these effects in more detail in Sec. IV C.

By employing Eqs. (17) and (18), we compute the anharmonicity and cross-Kerr interaction for scenarios where only the two lowest modes are allowed to hold excitations. Consequently, both modes exhibit two state-dependent anharmonicities and the cross-Kerr interaction between these two modes can be characterized by a single value. The results for this two-mode scenario are displayed in Fig. 5. Our observations indicate that within the two-mode framework, it is feasible to identify a set of parameters that distribute the nonlinearity relatively evenly across both modes. For example, using the parameters given in Table II, the anharmonicity of both modes remains above a 50-MHz threshold if the other mode is kept in the vacuum state. Furthermore, the cross-Kerr interaction energy lies around 200 MHz, peaking approximately at the same value of x_J as $\alpha_2(0, 0)$. However, it is evident that the anharmonicity of the lowest mode consistently surpasses that of the second mode. Transferring an excitation to a mode appears to have a diminishing effect on the anharmonicity of the other mode. The relative difference, between the anharmonicities with and without excitations present in the other mode, continues to increase with either increasing Josephson energy or characteristic impedance, even though the overarching trend is an increase in anharmonicity. Interestingly, the value of $\alpha_1(1, 0)$, however, begins to decrease once E_J or Z_c exceed a certain threshold. More details on this effect are found in Sec. IV C.
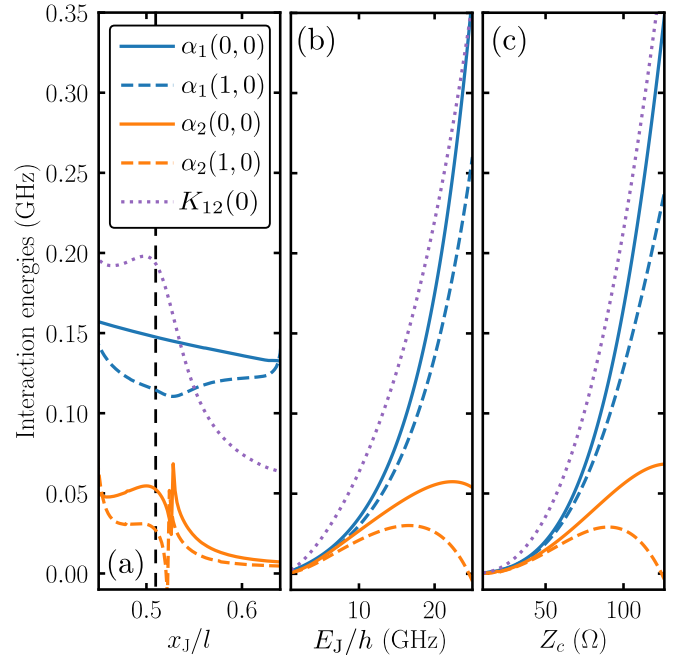

FIG. 5. Anharmonicities and cross-Kerr interaction energies for the two lowest modes of the unimon circuit as functions of (a) the location of Josephson junction x_J, (b) Josephson energy E_J, and (c) characteristic impedance Z_c of the CPW. The dashed vertical line in panel (a) indicates the value of x_J, which is subsequently used for the graphs in (b) and (c). The notation $\alpha_m(i, j)$ corresponds to the anharmonicity of the m:th mode ($m = 1, 2, 3$), with the other two modes having i and j excitations. The left argument (i) pertains to the lower mode of the two arguments. The cross-Kerr interaction is denoted by $K_{nm}(i)$, where n and m ($n, m = 1, 2, 3$) represent the modes between which the interaction is computed. The argument (i) equals to the number of excitations in the mode not primarily involved in the interaction. The simulations utilize the parameter values of Table II.

Our numerical calculations also extend to anharmonicities and cross-Kerr interactions for the three-mode scenario, the results of which are illustrated in Fig. 6. In our efforts to spread the nonlinearity across all three modes, we adjusted the location of the Josephson junction to $x_J = 0.62$ during the sweeps with respect to E_J and Z_c. In the case of three modes, the number of anharmonicities per mode increases to four, owing different combinations of excitations in the other two modes. Similarly, the number of cross-Kerr interactions for any pair of modes doubles, reflecting the influence exerted by the state of the remaining mode. The results highlight the challenge in discovering a set of parameters that ensures all anharmonicities exceed a 10-MHz threshold. As discussed in the context of the two-mode case, augmenting E_J or Z_c is not a feasible solution as it would result in a decrease in the lowest anharmonicity and cross-Kerr interaction. This outcome is visible for the anharmonicity $\alpha_2(1, 0)$ as shown in Figs. 6(b) and 6(c), and for the cross-Kerr interaction $K_{23}(1)$ as depicted in Figs. 6(e) and 6(f).

C. Analysis of Kerr-type terms

Although our model lends itself well to numerical simulations, it does not facilitate analytical derivations. This
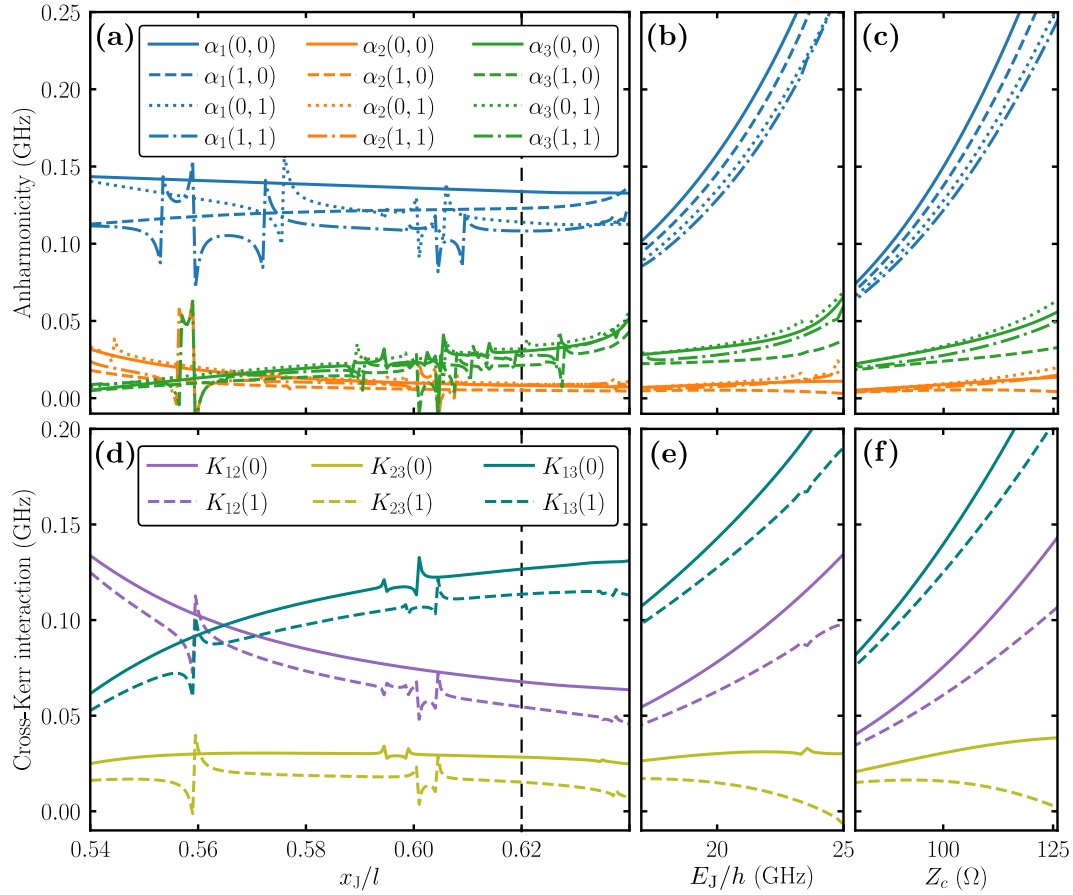
FIG. 6. [(a)–(c)] Anharmonicities and [(d)–(f)] cross-Kerr interaction energies for the three lowest modes of the unimon circuit as functions of [(a) and (d)] the Josephson junction location, [(b) and (e)] Josephson energy, and [(c) and (f)] characteristic impedance of the CPW. The notation $\alpha_m(i, j)$ and $K_{nm}(i)$ is defined in Eqs. (17) and (18), respectively, and in Fig. 5. For the parameter values that are not swept, we use Table II, except for the Josephson junction location set at $x_J/l = 0.62$, as marked by the vertical dashed line in (a) and (d).

limitation stems from the fact that the eigenstates of the single-mode unimon Hamiltonian seem not analytically solvable in general. Therefore, to analytically investigate the anharmonicities and cross-Kerr interactions, we make use of the harmonic-oscillator basis [31]. Here, $E_J^* = E_J \prod_{m=1}^{M+1} e^{-\lambda_m^2/2}$ represents the renormalized Josephson energy in the harmonic-oscillator basis [34,35], where $\lambda_m = 2\sqrt{E_{C,m}/(\hbar\omega_m)}$ signifies the zero-point fluctuations of the m:th mode. We refer to the different modes with the indices n, m, and k. Under these definitions, the analytical expressions for the anharmonicity and cross-Kerr interaction are expressed as

$$\alpha_m(N_n, N_k) = K_{mm}\left(1 - \sqrt{\frac{2K_{nn}}{E_J^*/h}}N_n - \sqrt{\frac{2K_{kk}}{E_J^*/h}}N_k\right.$$
$$\left. + \frac{K_{nk}}{E_J^*/h}N_nN_k\right), \qquad (19)$$

$$K_{nm}(N_k) = K_{nm}\left(1 - \sqrt{\frac{2K_{kk}}{E_J^*/h}}N_k\right), \qquad (20)$$

where N_m denotes the occupation number of the m:th mode and the self-Kerr and cross-Kerr interactions, when no excita-

tion present in other modes, are given by [29,31]

$$K_{mm} = \frac{E_J^*}{2h}\lambda_m^4 = \frac{8E_J^*}{h}\left(\frac{E_{C,m}}{\hbar\omega_m}\right)^2, \qquad (21)$$

$$K_{mn} = 2\sqrt{K_{mm}K_{nn}}, \quad \forall\, m \neq n. \qquad (22)$$

For more details on the derivation of these expressions, refer to Appendix G.

1. Modes in vacuum state

We begin our analysis with Eqs. (21) and (22), which represent the case without additional excitations in the system. To gain insight into the behavior of the self-Kerr interaction with respect to x_J, we represent K_{mm} in a more suggestive form, $K_{mm} \propto (E_{C,m}/\omega_m)^2$, where both $E_{C,m}$ and ω_m are dependent on x_J as depicted in Figs. 1(b) and 1(c).

Out of these two quantities, the effective charging energy $E_{C,m}$ is notably more sensitive to variations in x_J. As a result, $E_{C,m}$ largely determines the dependence of the anharmonicity of mode m on x_J. Interestingly, the dependence of $E_{C,m}$ on x_J follows the magnitude of the voltage discontinuity of mode m across the junction, suggesting that $E_{C,m}$ serves as an indicator of the coupling strength between mode m and the Josephson junction.

On the other hand, the transition frequency, $\omega_m/(2\pi)$, significantly influences the level of the anharmonicity for each mode. A higher transition frequency corresponds to reduced anharmonicity, as depicted in Fig. 1(d). Note that we do not consider the dependence of E_J^* on x_J in detail because it is relatively weak, as illustrated in Fig. 4(b).

The analytical form of the cross-Kerr interaction K_{nm} reveals a simple, yet important relationship with the self-Kerr interactions K_{mm} and K_{nn}. Specifically, the cross-Kerr interaction K_{mn} is twice the geometric mean of the self-Kerr interactions K_{mm} and K_{nn}. This indicates that the most efficient way to increase the cross-Kerr interaction between the modes, is to augment the self-Kerr interaction of both modes by an equal amount. Such conclusions regarding the behavior of the cross-Kerr interaction also applies for the parameter sweeps respect to E_J and Z_c.

We continue by examining the parameter sweep with respect to the Josephson energy E_J. In this case, the self-Kerr term of mode m can be expressed as $K_{mm} \propto \tilde{E}_J(E_{C,m}/\omega_m)^2$, highlighting the dependency of the self-Kerr on E_J. From the Fig. 3(b), we observe that the transition energies from the vacuum state E_{000} to the first excited states E_{100}, E_{010}, and E_{001} decrease with increasing E_J. Consequently, this leads to an increasing effect on K_{mm}, a trend also evident in the numerical results.

In addition, increase in Josephson energy has an enhancing effect on K_{mm}, even if the renormalization coefficient may decrease with increasing E_J. As a result, the self-Kerr interaction strength is anticipated to increase more rapidly with respect to E_J for the lowest mode than for the other modes, a pattern consistent with our numerical calculations. Another approach to reach this conclusion is by examining the quadratic part of the single-mode Hamiltonian in Eq. (9), given by $(E_{L,m} - E_J)\hat{\varphi}_m^2/2$. As $E_J/E_{L,m} \to 1$, this term approaches zero, while the magnitude of the nonlinear terms grows [27].

For the sweep with respect to Z_c, we expect similar behavior of the self-Kerr interaction to that for E_J. This is substantiated by the observation that when the operators in the auxiliary-mode Hamiltonian of Eq. (1) are rescaled, the outcomes of increasing either E_J or Z_c are approximately equal in the linear approximation (Appendix F). At the sweet spot, the linear effects are pronounced because the main cause of the increase in self-Kerr interaction is the cancellation of quadratic flux term as $E_J/E_{L,m} \to 1$. Nevertheless, higher-order terms indicate different behavior between the characteristic impedance Z_c and the Josephson energy E_J. Such disparities are particularly evident in the case of high-frequency modes, where the effect of the cancellation diminishes. For additional details, refer to Appendix F.

2. Effect of excitations

We turn our attention to the impact of excitations on both anharmonicity and cross-Kerr interactions. The origins of these effects can be traced back to nonlinear Hamiltonian terms, which are elaborated upon in Eqs. (19) and (20).

Introducing a single excitation into the k:th mode yields two notable outcomes. First, there is a negative correction to the anharmonicity of mode m. Second, a corresponding negative correction appears in the cross-Kerr interactions between modes m and n. The relative decline for both of these effects is captured mathematically as

$$\frac{\alpha_m(1,0) - K_{mm}}{K_{mm}} = \frac{K_{mn}(1) - K_{mn}}{K_{mn}} = -\sqrt{\frac{2K_{kk}}{E_J^*/h}}, \quad (23)$$

which reveals that the decrease caused by the excitation is at its maximum where K_{kk}/E_J^* attains its peak value. Furthermore, the equation suggests that a mode with a larger self-Kerr interaction induces a larger relative correction. These effects are evident in Fig. 5 for the anharmonicity and in Figs. 6(d)–6(f) for the cross-Kerr interaction.

Finally, we examine the anharmonicity when another excitation is introduced to the previously unoccupied mode n. The difference between this and the preceding case can be expressed as

$$\frac{\alpha_m(1,1) - \alpha_m(1,0)}{K_{mm}} = \lambda_n^2(\lambda_k^2 - 1). \quad (24)$$

The magnitude of the zero-point fluctuations in mode k, which is the mode excited for Eq. (23), determines the sign of the correction. Although the strength of the zero-point fluctuations in mode n does not influence the sign, it acts as a scaling coefficient, influencing the magnitude of the correction. Based on this analysis, the observed trends in Fig. 6 align well with our expectations. For a majority of the parameter configurations, the lowest mode shows that $\alpha_1(1,1)$ is the smallest anharmonicity. For the other two modes, we consistently find that $\alpha_m(1,1) > \alpha_m(1,0)$. From a qualitative perspective this makes sense since the lowest mode has the largest zero-point fluctuation. However, quantitatively this behavior is not explained by Eq. (24), since positive correction requires $\lambda_1^2 > 1$ which is not satisfied in this case.

It is important, however, to recognize the limits of this analytical methodology. Although instrumental in elucidating the qualitative behavior of Kerr-type interactions, the approach does not encompass transverse-type or other rotating-wave interactions. These interactions may be significant, especially in systems with notable nonlinearity.

V. CONCLUSIONS

In this work, we explored the effects arising from the multimode nature of the single-junction unimon circuit. Whereas our primary focus was on the impact of the high-lying modes on the lowest mode, we also investigated the influence of the nonlinearity on other modes for different locations of the Josephson junction. To facilitate our study, we developed a theory of multimode unimon circuits. This framework was leveraged to determine the energy spectrum for several low-lying modes using numerical diagonalization in the low-energy subspace.

Our model, referred to as multimode model, markedly differs from the one presented in Ref. [44] that describes the multimode physics in Josephson-junction array fluxonium circuits. While the effectiveness of their model relies on the decoupling of the qubit mode from all other modes, the distinctiveness of our model arises from the large energy separation between the qubit subspace and the high-frequency

modes, which is a consequence of the CPW structure. Furthermore, the methods of numerical diagonalization for fluxonium qubits presented in Refs. [14,33] differ from our approach, particularly with respect to the chosen basis. In Ref. [14], diagonalization is executed in the normal-mode flux basis, which enforces a mode cutoff that includes only two modes. On the other hand, the Hamiltonian in Ref. [33] is expressed in the harmonic-oscillator basis, leading to a less efficient convergence of the low-energy eigenstates when compared to our unimon basis. By adjusting the choice of basis to the problem at hand, we expect that the presented model is also applicable to a class of multimode qubits known as noise-protected qubits [22–24,45–47].

Our findings reveal that multimode effects introduce significant corrections to both the transition frequency and anharmonicity of the unimon qubit. Utilizing our multimode model, the decrease in anharmonicity can be as much as 30% when the junction is centrally located, with more pronounced effects observed at other positions. We also showed that by solely considering the vacuum states, the multimode effects can be condensed into a single coefficient, leading to a renormalization of the Josephson energy. The decrease in the anharmonicity owing to the renormalization can be compensated by the choice of an increased bare Josephson energy. Compared to the single-mode model introduced in Ref. [27], this method seamlessly incorporates certain multimode effects without greatly increasing the required computational resources.

A numerical comparison of the unimon models described in this study with those presented in Ref. [27] indicates that the multimode model not only matches the accuracy of the best existing models but also surpasses them in efficiency. This advantage is particularly notable at the sweet spots, where the multimode model achieves its highest accuracy. Although the multimode model accurately fits the lowest-frequency mode of the unimon circuit, determining its efficacy in describing modes beyond the lowest one remains an important question for future research.

We found that the second and third modes present a diverse nonlinearity profile, but their peaks do not coincide. This misalignment poses a challenge in identifying an operational regime where all three of the lowest modes exhibit substantial nonlinearity. Yet, for the first and second modes, we identified a position with notable nonlinearity in both.

Our work significantly expands upon the prior theoretical descriptions of the unimon [27] by introducing a theoretical framework to systematically investigate the multimode physics of the unimon circuit and its potential applications. An interesting application for unimon circuits is to encode multiple qubits into a single device in the spirit of multimon qubits [37–39]. However, although we identified parameter configurations where two modes simultaneously exhibit significant nonlinearity, we did not find promising parameters for particularly high-fidelity qubits. In our future research, we aim to apply our theoretical framework for more complex unimon circuits. For example, by implementing a ring-like geometry and adding more junctions, we expect to witness behavior similar to transmon-based multimons, characterized by a relatively uniform distribution of nonlinearity among the modes with high intrinsic anharmonicity.

APPENDIX A: DERIVATION OF AUXILIARY-MODE HAMILTONIAN

Here, we derive the auxiliary-mode Hamiltonian that was used as a starting point for the theoretical considerations in Sec. II of the main text.

1. Equations of motion of the distributed-element circuit

We begin by formulating the total Lagrangian for the continuous distributed-element circuit, presented as

$$L_{\text{tot}} = \int_{-l}^{l} \mathcal{L}\left(\psi, \frac{\partial\psi}{\partial x}, \frac{\partial\psi}{\partial t}; x, t\right) dx + L(\Psi, \dot{\Psi}; t), \quad \text{(A1)}$$

where we have defined

$$\psi(x, t) = \begin{cases} \psi_1(x, t), & -l < x < x_{\text{J}} \\ \psi_2(x, t), & x_{\text{J}} < x < l \end{cases}, \quad \text{(A2)}$$

which describes the flux of the grounded CPW resonator and $\Psi(t) = \psi_2(x_{\text{J}}, t) - \psi_1(x_{\text{J}}, t)$ denotes the flux difference across the Josephson junction. The Lagrangian density $\mathcal{L}$ of the CPW and the Lagrangian L describing the flux across the junction are defined as [48]

$$\mathcal{L} = \frac{C_l}{2}[\dot{\psi}(x, t)]^2 - \frac{1}{2L_l}[\partial_x \psi(x, t)]^2$$

$$L = \frac{C_{\text{J}}}{2}[\dot{\Psi}(t)]^2 + E_{\text{J}} \cos\left\{\frac{2\pi}{\Phi_0}[\Psi(t) - \Phi_{\text{diff}}]\right\}, \quad \text{(A3)}$$

where Φ_{diff} is the total flux difference across the loops and the system obeys the boundary condition $\psi(-l, t) = \psi(l, t) = 0$. We apply the Hamilton's principle [49] to minimize the action, defined as $S = \int_{t_1}^{t_2} L_{\text{tot}} dt$. This is done by requiring that $\delta S = 0$. The variations of the action can expressed as

$$\delta S = \delta \int_{t_1}^{t_2} \left[\int_{-l}^{l} \mathcal{L}\left(\psi, \frac{\partial\psi}{\partial x}, \frac{\partial\psi}{\partial t}; x, t\right) dx + L(\Psi, \dot{\Psi}; t) \right] dt$$

$$= \int_{t_1}^{t_2} dt \int_{-l}^{x_{\text{J}}} dx \left[\frac{\partial\mathcal{L}}{\partial\psi_1} - \frac{\partial}{\partial t}\frac{\partial\mathcal{L}}{\partial\dot{\psi}_1} - \frac{\partial}{\partial x}\frac{\partial\mathcal{L}}{\partial(\partial_x\psi_1)} \right] \delta\psi_1$$

$$+ \int_{t_1}^{t_2} dt \int_{x_{\text{J}}}^{l} dx \left[\frac{\partial\mathcal{L}}{\partial\psi_2} - \frac{\partial}{\partial t}\frac{\partial\mathcal{L}}{\partial\dot{\psi}_2} - \frac{\partial}{\partial x}\frac{\partial\mathcal{L}}{\partial(\partial_x\psi_2)} \right] \delta\psi_2$$

$$+ \int_{t_1}^{t_2} dt \left[\frac{\partial L}{\partial\psi_{\text{J},1}} - \frac{\partial}{\partial t}\frac{\partial L}{\partial\dot{\psi}_{\text{J},1}} + \frac{\partial\mathcal{L}}{\partial(\partial_x\psi_1)}\bigg|_{x=x_{\text{J}}} \right] \delta\psi_{\text{J},1}$$

$$+ \int_{t_1}^{t_2} dt \left[\frac{\partial L}{\partial\psi_{\text{J},2}} - \frac{\partial}{\partial t}\frac{\partial L}{\partial\dot{\psi}_{\text{J},2}} - \frac{\partial\mathcal{L}}{\partial(\partial_x\psi_2)}\bigg|_{x=x_{\text{J}}} \right] \delta\psi_{\text{J},2},$$

$$\text{(A4)}$$

which results into a set of Euler-Lagrange equations, defined as

$$\frac{\partial \mathcal{L}}{\partial \psi_i} - \frac{\partial}{\partial t}\frac{\partial \mathcal{L}}{\partial(\partial \psi_i/\partial t)} - \frac{\partial}{\partial x}\frac{\partial \mathcal{L}}{\partial(\partial \psi_i/\partial x)} = 0, \qquad (A5)$$

$$\frac{\partial L}{\partial \psi_{J,i}} - \frac{\partial}{\partial t}\frac{\partial L}{\partial \dot{\psi}_{J,i}} - (-1)^i\frac{\partial \mathcal{L}}{\partial(\partial \psi_i/\partial x)}\bigg|_{x=x_J} = 0, \qquad (A6)$$

where $i \in \{1, 2\}$ and $\psi_{J,i} \equiv \psi_i(x_J, t)$. To utilize the Euler-Lagrange framework, we derive the subsequent equations of motion

$$\partial_x^2 \psi_i(x, t) = \frac{1}{v^2}\partial_t^2 \psi_i(x, t), \quad i \in \{1, 2\}, \qquad (A7)$$

$$C_J\ddot{\Psi}(t) + I_c \sin\left\{\frac{2\pi}{\Phi_0}[\Psi(t) - \Phi_{\text{diff}}]\right\}$$
$$= \frac{1}{L_l}\partial_x \psi_i(x, t)\big|_{x=x_J}, \quad i \in \{1, 2\}, \qquad (A8)$$

where the phase velocity is denoted as $v = 1/\sqrt{L_l C_l}$.

2. Variable elimination in frequency domain

Our interest is to eliminate the variable ψ_i and express the equation of motion solely with the variable Ψ. In order to achieve this, we move to a frequency domain by using Fourier transformation, which is defined as

$$\tilde{f}(\omega) = \mathcal{F}[f](\omega) = \int_{-\infty}^{\infty} dt \exp(-i\omega t)f(t), \qquad (A9)$$

where $f : \mathbb{R} \to \mathbb{R}$, $f \in L_2[\mathbb{R}]$. Starting with the wave equation in Eq. (A7), we apply Eq. (A9) and a property $\mathcal{F}[\partial_t f](\omega) = i\omega\tilde{f}(\omega)$ to express the wave equation in angular frequency domain as

$$\partial_x^2 \tilde{\psi}_i(x, \omega) = -\frac{\omega^2}{v^2}\tilde{\psi}_i(x, \omega), \quad i \in \{1, 2\}, \qquad (A10)$$

where $\tilde{\psi}_i(x, \omega) \equiv \mathcal{F}[\psi_i](\omega)$. The solution for the wave equation in angular frequency domain is

$$\tilde{\psi}_i(x, \omega) = A_i^{(s)}(\omega)\sin(k_\omega x) + A_i^{(c)}(\omega)\cos(k_\omega x), \qquad (A11)$$

where the wave number is denoted as $k_\omega = \omega/v$.

We can determine the coefficients $A_i^{(s)}$ and $A_i^{(c)}$ by taking the Fourier transformation of Eq. (A8), which results in

$$\frac{1}{L_l}\partial_x \tilde{\psi}_2(x_J, \omega) = \frac{1}{L_l}\partial_x \tilde{\psi}_1(x_J, \omega). \qquad (A12)$$

This condition ensures that the current across the Josephson junction is continuous. In addition, incorporating the boundary conditions of the grounded CPW and the flux difference across the junction, we can extract the frequency-dependent coefficients as

$$A_1^{(s)}(\omega) = -\frac{1}{2}\tilde{\Psi}(\omega)\frac{\cos[k_\omega(x_J - l)]}{\sin(k_\omega l)}, \qquad (A13)$$

$$A_1^{(c)}(\omega) = -\frac{1}{2}\tilde{\Psi}(\omega)\frac{\cos[k_\omega(x_J - l)]}{\cos(k_\omega l)}, \qquad (A14)$$

$$A_2^{(s)}(\omega) = -\frac{1}{2}\tilde{\Psi}(\omega)\frac{\cos[k_\omega(x_J + l)]}{\sin(k_\omega l)}, \qquad (A15)$$

$$A_2^{(c)}(\omega) = \frac{1}{2}\tilde{\Psi}(\omega)\frac{\cos[k_\omega(x_J + l)]}{\cos(k_\omega l)}. \qquad (A16)$$

By inserting the derived coefficients into Eqs. (A11) and (A12), we obtain

$$\frac{1}{L_l}\partial_x \tilde{\psi}_i(x_J, \omega) = -\tilde{K}(\omega)\tilde{\Psi}(\omega), \qquad (A17)$$

where the kernel function is defined as

$$\tilde{K}(\omega) = \frac{k_\omega \cos[k_\omega(x_J + l)]\cos[k_\omega(x_J - l)]}{L_l \sin(2k_\omega l)}. \qquad (A18)$$

This kernel $\tilde{K}$ encapsulates the intricate relationship between the Josephson junction and the CPW resonator, enabling us to focus solely on the Ψ variable.

Switching back to the time domain with the help of the inverse Fourier transformation, gives rise to the integro-differential equation

$$C_J\ddot{\Psi}(t) + I_c \sin\left\{\frac{2\pi}{\Phi_0}[\Psi(t) - \Phi_{\text{diff}}]\right\}$$
$$+ \int_{-\infty}^{\infty} K(t - \tau)\Psi(\tau)d\tau = 0. \qquad (A19)$$

Although this equation provides a stepping stone into the classical dynamics of the system, our end goal is to formulate the quantized Hamiltonian. For this purpose, we continue in the frequency domain, aiming to replace the kernel function with resonator eigenmodes.

3. Pole expansion of the kernel function

To carry out a pole decomposition of the kernel $\tilde{K}$, we treat ω as a complex variable. This lets us use a Mittag-Leffler variant to express the kernel function [50]. The decomposition is expressed as

$$\tilde{K}(\omega) = \sum_{n=0}^{\infty} \frac{d^n\tilde{K}(\omega)}{d\omega^n}\bigg|_{\omega=0}\frac{\omega^n}{n!}$$
$$+ \sum_{m=1}^{M}\left\{\frac{2r_m\Omega_m}{\omega^2 - \Omega_m^2} + \frac{r_m}{\Omega_m}\sum_{n=0}^{\infty}[1 + (-1)^n]\left(\frac{\omega}{\Omega_m}\right)^n\right\}, \qquad (A20)$$

where M is a positive integer that denotes the number modes and the location of the poles, $\Omega_m = \pi v m/(2l)$, correspond to the harmonic modes of the resonator as can be observed from Eq. (A18). The residues for each pole are denoted as $r_m = \text{r}[\tilde{K}(\omega), \Omega_m]$. The first summation in Eq. (A18) represents the Maclaurin series, providing an estimate of $\tilde{K}(\omega)$ at low frequencies. The second summation term is introduced by adding zeros in a form of geometric series as

$$0 = \frac{r_m}{\omega - \Omega_m} + \frac{r_m}{\Omega_m}\sum_{n=0}^{\infty}\left(\frac{\omega}{\Omega_m}\right)^n, \qquad (A21)$$

which is valid under the condition $|\omega/\Omega_m| < 1$. The residues of each pole are given by

$$r_m = \frac{\Omega_m \cos^2\left(\frac{\Omega_m x_J}{v} + \frac{\pi}{2}m\right)}{2lL_l}, \quad (A22)$$

which satisfies $r_m = -r_{-m}$.

4. Introducing auxiliary modes

Using the pole decomposition form of the kernel function, the convolution term in Eq. (A19) can be expressed as

$$\int_{-\infty}^{\infty} K(t-\tau)\Psi(\tau)d\tau$$

$$= \mathcal{F}^{-1}\left[\sum_{m=1}^{M}\frac{2r_m\Omega_m}{\omega^2-\Omega_m^2}\tilde{\Psi}(\omega)\right](t)$$

$$+ \sum_{\substack{n=0 \\ \text{even } n}}^{\infty}\left\{\frac{1}{n!}\frac{d^n\tilde{K}(\omega)}{d\omega^n}\bigg|_{\omega=0} + \sum_{m=1}^{M}\frac{2r_m}{\Omega_m^{n+1}}\right\}(-i)^n\partial_t^n\Psi(t)$$

$$\approx \left[\tilde{K}(0) + \sum_{m=1}^{M}\frac{2r_m}{\Omega_m}\right]\Psi(t) - \left[\frac{\tilde{K}''(0)}{2} + \sum_{m=1}^{M}\frac{2r_m}{\Omega_m^3}\right]\ddot{\Psi}(t)$$

$$+ \mathcal{F}^{-1}\left[\sum_{m=1}^{M}\frac{2r_m\Omega_m}{\omega^2-\Omega_m^2}\tilde{\Psi}(\omega)\right](t), \quad (A23)$$

where $\mathcal{F}^{-1}$ denotes the inverse Fourier transform. We have also used the convolution theorem, defined as

$$\int_{-\infty}^{\infty} f(\tau)g(t-\tau)d\tau = \mathcal{F}^{-1}[\tilde{f}\tilde{g}](t), \quad (A24)$$

and the fact that contribution from odd time derivatives of flux is zero. This is evidenced by the fact that, if n is odd, both $d^n\tilde{K}(\omega)/(d\omega^n)|_{\omega=0}$ and the latter term in the second row of Eq. (A20) are zero.

In addition, since the only lumped element which depends on time-derivatives of flux is capacitance, we may utilize the low-frequency assumption made with the pole expansion to approximate the convolution by neglecting time derivatives $\partial_t^n\Psi(t)$ when $n > 2$. Interestingly, this low-frequency approximation made in the convolution expression in Eq. (A23) becomes exact in the limit of $M \to \infty$. In this limit, Mittag-Leffler theorem [51] allows us to express the kernel in Eq. (A20) as

$$\tilde{K}(\omega) = \tilde{K}(0) + \sum_{m=1}^{\infty}\left\{\frac{2r_m\Omega_m}{\omega^2-\Omega_m^2} + \frac{2r_m}{\Omega_m}\right\}, \quad (A25)$$

where all contributions from kernel $\tilde{K}(\omega)$ to the time derivatives in the convolution term [Eq. (A23)] vanish. Similar technique has been previously utilized in the context of network synthesis of prescribed impedance functions [52].

The approximation of convolution, as given in Eq. (A23), leads us to a more tractable expression for the full equation of

motion in Eq. (A19) which takes the form

$$C_{\text{eff}}\ddot{\Psi}(t) + L_{\text{eff}}^{-1}\Psi(t) + I_c\sin\left\{\frac{2\pi}{\Phi_0}[\Psi(t) - \Phi_{\text{diff}}]\right\}$$

$$= -\mathcal{F}^{-1}\left[\sum_{m=1}^{M}\frac{2r_m\Omega_m}{\omega^2-\Omega_m^2}\tilde{\Psi}(\omega)\right](t), \quad (A26)$$

where we used the definitions for C_{eff} and L_{eff} given in the Eqs. (2) and (3) of the main text.

To handle the temporally nonlocal term, we employ a set of auxiliary modes, denoted as

$$\chi_m(t) = \mathcal{F}^{-1}\left[\sqrt{\frac{2r_m\Omega_m}{C_{\text{eff}}}}\frac{\tilde{\Psi}(\omega)}{\omega^2-\Omega_m^2}\right](t). \quad (A27)$$

This helps us to express Eq. (A26) as

$$C_{\text{eff}}\ddot{\Psi}(t) + L_{\text{eff}}^{-1}\Psi(t) + \sum_{m=1}^{M}\xi_m\chi_m(t)$$

$$= -I_c\sin\left\{\frac{2\pi}{\Phi_0}[\Psi(t) - \Phi_{\text{diff}}]\right\}, \quad (A28)$$

where $\xi_m = \sqrt{2r_m\Omega_m C_{\text{eff}}}$. For a complete description of the system dynamics, we derive the equations for each auxiliary mode.

We begin by taking the second order time derivative of the Eq. (A27), which gives us

$$\ddot{\chi}_m(t) = \sqrt{\frac{2r_m\Omega_m}{C_{\text{eff}}}}\mathcal{F}^{-1}\left[\frac{\omega^2}{\omega^2-\Omega_m^2}\tilde{\Psi}(\omega)\right](t). \quad (A29)$$

By utilizing the convolution theorem in Eq. (A24) and relations

$$\mathcal{F}^{-1}\left[\frac{\omega^2}{\omega^2-\Omega_m^2}\right](t) = \delta(t) - \frac{\Omega_m}{2}\text{sgn}(t)\sin(\Omega_m t), \quad (A30)$$

$$\mathcal{F}[\text{sgn}(t)\sin(\Omega_m t)](\omega) = -\frac{2\Omega_m}{\omega^2-\Omega_m^2}, \quad (A31)$$

we obtain the equations of motion for the auxiliary modes, which can be expressed as

$$C_{\text{eff}}\ddot{\chi}_m(t) + \xi_m\Psi(t) + C_{\text{eff}}\Omega_m^2\chi_m(t) = 0. \quad (A32)$$

By introducing auxiliary modes, we have successfully eliminated the need to compute temporal convolutions.

5. Classical treatment of the dc flux

In the pursuit of computing the normal modes of the system, it is convenient to redefine the fluxes such that they vanish at the minima of their effective potentials. To this end, we define the shifted flux and the auxiliary variables as follows: $\Psi'(t) = \Psi(t) - \Phi_{\text{diff}} + \phi_0$, where the dc flux component ϕ_0 is separated from the dynamic component $\Psi'(t)$. Similarly, for the auxiliary modes, we define $\chi_m'(t) = \chi_m(t) + x_m$.

Substituting these into our earlier equations, we obtain

$$
C_{\text{eff}} \ddot{\Psi}'(t) + L_{\text{eff}}^{-1} \Psi'(t) + \sum_{m=1}^{M} \xi_m \chi'_m(t)
$$
$$
+ I_c \sin \left\{ \frac{2\pi}{\Phi_0} [\Psi'(t) - \phi_0] \right\} + I_c \sin \left(\frac{2\pi \phi_0}{\Phi_0} \right)
$$
$$
= -L_{\text{eff}}^{-1} (\Phi_{\text{diff}} - \phi_0) - \sum_{m=1}^{M} \xi_m x_m + I_c \sin \left(\frac{2\pi \phi_0}{\Phi_0} \right)
$$

(A33)

$$
C_{\text{eff}} \ddot{\chi}'_m(t) + \xi_m \Psi'(t) + C_{\text{eff}} \Omega_m^2 \chi'_m(t)
$$
$$
= -\xi_m (\Phi_{\text{diff}} - \phi_0) - C_{\text{eff}} \Omega_m^2 x_m.
$$

(A34)

It is clear that the right side of these equations captures the time-independent behavior, with the left side containing time-dependent part of the system.

Conveniently, the time-independent parts of Eqs. (A33) and (A34) can be solved independently from the time-dependent parts, giving us a set of new equations

$$
I_c \sin \left(\frac{2\pi \phi_0}{\Phi_0} \right) - \frac{\Phi_{\text{diff}} - \phi_0}{L_{\text{eff}}} = \sum_{m=1}^{M} \xi_m x_m
$$

(A35)

$$
C_{\text{eff}} \Omega_m^2 x_m = -\xi_m (\Phi_{\text{diff}} - \phi_0).
$$

(A36)

From these equations, by eliminating the variables x_m, we obtain the relation

$$
\frac{\Phi_{\text{diff}} - \phi_0}{2lL_l} - I_c \sin \left(\frac{2\pi \phi_0}{\Phi_0} \right) = 0.
$$

(A37)

This equation links the dc flux across our junction to the external magnetic flux, encapsulating the dc flux behavior of our system in the presence of an external magnetic influence. Note that the Eq. (A37) becomes multi-valued if $2lL_l/L_J > 1$ [53–55], a parameter region we aim to avoid.

6. Finding the Hamiltonian and quantization

The Lagrangian that corresponds to the left side of Eqs. (A33) and (A34) can be expressed as

$$
\mathcal{L}_{\text{aux}} = \frac{C_{\text{eff}} \dot{\Psi}'^2}{2} - \frac{\Psi'^2}{2L_{\text{eff}}} + E_J \cos \left(\frac{2\pi}{\Phi_0} [\Psi' - \phi_0] \right)
$$
$$
+ \sum_{m=1}^{M} C_{\text{eff}} \left[\frac{\dot{\chi}'^2_m}{2} - \Omega_m^2 \frac{\chi'^2_m}{2} \right] - \sum_{m=1}^{M} \xi_m \chi'_m \Psi'
$$
$$
- \frac{\Psi'}{2lL_l} (\Phi_{\text{diff}} - \phi_0),
$$

(A38)

where we omitted the explicit temporal dependencies for brevity.

In order to transition to the Hamiltonian formalism, we define the conjugate momenta associated with Ψ' and χ'_m as

$$
Q' = C_{\text{eff}} \dot{\Psi}', \quad \Xi'_m = C_{\text{eff}} \dot{\chi}'_m.
$$

(A39)

Using a Legendre transformation and subsequent quantization, we obtain

$$
\hat{H}_{\text{aux}} = \frac{\hat{Q}'^2}{2C_{\text{eff}}} + \frac{\hat{\Psi}'^2}{2L_{\text{eff}}} + \frac{\hat{\Psi}'}{2lL_l} (\Phi_{\text{diff}} - \phi_0)
$$
$$
+ \sum_{m=1}^{M} \left[\frac{\hat{\Xi}'^2_m}{2C_{\text{eff}}} + C_{\text{eff}} \Omega_m^2 \frac{\hat{\chi}'^2_m}{2} \right] + \sum_{m=1}^{M} \xi_m \hat{\chi}'_m \hat{\Psi}'
$$
$$
- E_J \cos \left[\frac{2\pi}{\Phi_0} (\hat{\Psi}' - \phi_0) \right],
$$

(A40)

where the associated quantum operators obey the commutation relations $[\hat{\Psi}', \hat{Q}'] = i\hbar$ and $[\hat{\chi}'_n, \hat{\Xi}'_m] = i\hbar \delta_{nm}$ with all other commutators giving zero. Omission of primes in this Hamiltonian leads to the auxiliary-mode Hamiltonian in Eq. (1).

7. Comparison with prior models

In Ref. [27], an equivalent Hamiltonian is derived by employing path integrals. In this path-integral-based approach, the degrees of freedom of the CPW are eliminated using the path integral formalism, leading to a temporally nonlocal kernel function similar to that in Eq. (A18). The resulting Euclidean action is then compared to a specifically chosen trial action, which has the same form as the corresponding action for the Lagrangian in Eq. (A38). By equating these actions, one can derive a Hamiltonian for the system that aligns with the auxiliary-mode Hamiltonian presented in Eq. (1).

Despite leading to the same end result, the alternative derivation presented here offers two main advantages. First, it avoids the conceptually challenging path-integral technique. Second, the auxiliary-mode Lagrangian, as expressed in Eq. (A38), can be derived without resorting to a trial action. This approach simplifies the process, enabling one to reach the final result without requiring prior intuition about its form.

The model 1 in Ref. [27] departs from both of these approaches. Contrary to the derivation presented above, which relies on pole expansion in the frequency domain to identify a set of auxiliary modes for easy conversion into a Hamiltonian representation, the model 1 approach focuses on identifying normal modes from the linearized equations of motion and then constructing the Hamiltonian using these normal-mode coordinates. However, a major disadvantage of this approach is that the normal-mode frequencies cannot be expressed analytically, resulting in a Hamiltonian that lacks an exact analytical form. In contrast, the auxiliary-mode Hamiltonian in Eq. (1) does not encounter this issue. This advantage arises because the kernel function is analytically expressible through the pole expansion detailed in Eq. (A20), where the location of the poles corresponds exactly with CPW resonator mode frequencies. This alignment is not surprising, as the kernel function describes how the flux across the Josephson junction is influenced by the CPW structure, as evidenced by the relation in Eq. (A17).

APPENDIX B: LINEARIZATION OF AUXILIARY-MODE HAMILTONIAN

In this Appendix, we supplement the derivation of the normal-mode representation of the auxiliary-mode

Hamiltonian $\hat{H}_{\text{aux}}$ with details that were omitted in the Sec. II A of the main text.

The linear and nonlinear parts of the auxiliary-mode Hamiltonian are defined as

$$\hat{H}_{\text{lin}} = \frac{\hat{Q}^2}{2C_{\text{eff}}} + \frac{1}{2}\left[\frac{1}{L_{\text{eff}}} + \frac{\cos(2\pi\phi_0/\Phi_0)}{L_J}\right]\hat{\Psi}^2$$

$$+ \sum_{m=1}^{M}\left[\frac{\hat{\Xi}_m^2}{2C_{\text{eff}}} + \frac{1}{2}C_{\text{eff}}\Omega_m^2\hat{\chi}_m^2 + \xi_m\hat{\chi}_m\hat{\Psi}\right], \quad (B1)$$

$$\hat{H}_{\text{nl}} = -E_J\cos\left[\frac{2\pi}{\Phi_0}(\hat{\Psi} - \phi_0)\right] + I_c\sin\left(\frac{2\pi\phi_0}{\Phi_0}\right)\hat{\Psi}$$

$$- \frac{1}{2L_J}\cos\left(\frac{2\pi\phi_0}{\Phi_0}\right)\hat{\Psi}^2, \quad (B2)$$

where the last two terms cancel out the first- and second-order contributions from the cosine function, consequently showing that $\hat{H}_{\text{nl}}$ contributes to fully nonlinear dynamics. This becomes particularly clear if the trigonometric identity $\cos(x - y) = \cos x \cos y + \sin x \sin y$ is applied. We also note that the dc magnetic flux offset across the junction ϕ_0 and the half difference of the external magnetic flux Φ_{diff} are connected through a relation

$$\frac{\Phi_{\text{diff}} - \phi_0}{2lL_l} - I_c\sin\left(\frac{2\pi\phi_0}{\Phi_0}\right) = 0, \quad (B3)$$

which is used in Eq. (B1). As elaborated upon in Appendix A, this relation arises from the time-independent part of the classical Lagrange equation for the system. Specifically, it demonstrates how the dc flux difference across the Josephson junction is influenced by the difference in external fluxes passing through the two loops.

In a matrix form the linear part is expressed as

$$\hat{H}_{\text{lin}} = \frac{1}{2}\mathbf{Q}^\dagger\mathbf{C}^{-1}\mathbf{Q} + \frac{1}{2}\mathbf{V}^\dagger\mathbf{L}^{-1}\mathbf{V}, \quad (B4)$$

where the flux vector $\mathbf{V}$ is defined as $[\mathbf{V}]_0 = \hat{\Psi}$, $[\mathbf{V}]_m = \hat{\chi}_m$, $m \in \{1, 2, \ldots, M\}$ and correspondingly the charge vector $\mathbf{Q}$ is defined as $[\mathbf{Q}]_0 = \hat{Q}$, $[\mathbf{Q}]_m = \hat{\Xi}_m$, $m \in \{1, 2, \ldots, M\}$. Since there is no capacitive coupling present in the system, the inverse of the capacitance matrix is simply $[\mathbf{C}^{-1}]_{nn} = 1/C_{\text{eff}}$, $n \in \{0, 1, 2, \ldots, M\}$. For the inverse of the inductance matrix, the nonzero elements are defined as $[\mathbf{L}^{-1}]_{00} = L_{\text{eff}}^{-1} + \cos(\varphi_0)/L_J$, $[\mathbf{L}^{-1}]_{mm} = C_{\text{eff}}\Omega_m^2$ and $[\mathbf{L}^{-1}]_{0m} = [\mathbf{L}^{-1}]_{m0} = \xi_m$, $m \in \{1, 2, \ldots, M\}$.

Such matrix can be diagonalized by introducing an unitary matrix $\mathbf{U}$ that satisfies $\mathbf{D} = \mathbf{U}^T\mathbf{L}^{-1}\mathbf{U}$, where the matrix $\mathbf{D}$ is diagonal. By utilizing this, the Hamiltonian in Eq. (B4) can be expressed as

$$\hat{H}_{\text{lin}} = \frac{1}{2}\mathbf{q}^\dagger\mathbf{C}^{-1}\mathbf{q} + \frac{1}{2}\mathbf{v}^\dagger\mathbf{D}\mathbf{v}, \quad (B5)$$

where $[\mathbf{q}]_n = [\mathbf{U}^\dagger\mathbf{Q}]_n = \hat{q}_n$, $n \in \{0, 1, 2, \ldots, M\}$ and $[\mathbf{v}]_n = [\mathbf{U}^\dagger\mathbf{V}]_n = \hat{\phi}_n$, $n \in \{0, 1, 2, \ldots, M\}$.

Finally, the linear part of the Hamiltonian can be expressed as

$$\hat{H}_{\text{lin}} = \sum_{m=0}^{M}\left[\frac{\hat{q}_m^2}{2C_{\text{eff}}} + \frac{1}{2}C_{\text{eff}}\omega_m^2\hat{\phi}_m^2\right], \quad (B6)$$

where the normal-mode frequencies are denoted as $\omega_m/(2\pi)$. Furthermore, the normal-mode decompositions for operators

$\hat{\Psi}$ and $\hat{\chi}_m$ take the form

$$\hat{\Psi} = \sum_{m=1}^{M+1}[\mathbf{U}]_{0,m-1}\hat{\phi}_m, \quad \hat{\chi}_m = \sum_{n=1}^{M+1}[\mathbf{U}]_{m,n-1}\hat{\phi}_n, \quad (B7)$$

and thus, the coefficients c_m in Eq. (5) of the main text are given by $c_m = [\mathbf{U}]_{0,m-1}$.

APPENDIX C: DIVISION TO SINGLE-MODE AND INTERACTION PARTS

Starting with the assumption that $\varphi_0 = \pi$ and inspecting Eq. (11) of the main text, we note that only the term containing only cosines is a single-mode term. All other terms involve products of sines, which introduce coupling between the modes. We proceed by expressing the product of cosines as

$$\prod_{i=1}^{N}[1 + (\cos\hat{\varphi}_i - 1)]$$

$$= 1 + \sum_{k=1}^{N}(\cos\hat{\varphi}_i - 1) + \sum_{k=2}^{N}\sum_{\substack{A\subseteq\{1,\ldots,N\}\\|A|=k}}\prod_{i\in A}(\cos\hat{\varphi}_i - 1), \quad (C1)$$

The significance of $(\cos\hat{\varphi}_m - 1)$ arises from the cancellation of the constant term. Consequently, the last summation term inevitably includes only interaction terms, whereas the second summation term holds the single-mode contribution. By applying the above steps to Eq. (10), the single-mode contributions conveniently cancel each other out, and hence only interaction terms remain.

APPENDIX D: SCALING OF THE RENORMALIZATION COEFFICIENT

Here, we study the scaling properties of the renormalization coefficient $\tilde{E}_J/E_J$ in more detail. We put forward a convincing argument that the mode cutoff frequency used in the multimode model of the main text is reasonable.

In Fig. 7, we show the renormalization coefficient for the lowest mode as a function of the total number of modes that are coupled to the Josephson junction. Importantly, the renormalization coefficient appears to converge to a value slightly below 0.90. This supports our choice of the mode cutoff frequency, based on the superconducting gap, which yielded a renormalization coefficient of approximately $\tilde{E}_J/E_J \approx 0.90$ (see Sec. III in the main text).

To understand this behavior, we consider the renormalization coefficient expressed in the harmonic-oscillator basis as

$$E_J^*/E_J = \prod_{m=2}^{M}e^{-\lambda_m^2/2}, \quad \lambda_m = 2\sqrt{\frac{E_{C,m}}{\hbar\omega_m}}, \quad (D1)$$

where λ_m denotes the zero-point fluctuations of the mode m. In the exponent, both the inverse of the mode angular eigenfrequency and the effective charging energy are present, which are both depicted in the inset of Fig. 7 as functions of mode number m. Due to the CPW structure, the eigenfrequency scales as $\sim 1/m$. This scaling alone would lead to $E_J^*/E_J \sim 1/M$, causing the renormalization coefficient to
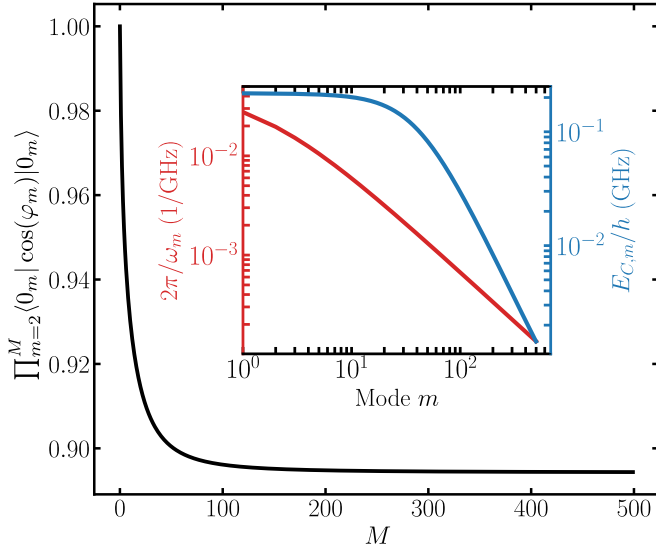
FIG. 7. Renormalization coefficient $\tilde{E}_J/E_J$ ($M_0 = 1$) as a function of the total number of modes M (black curve). The inset shows the inverse of the mode eigenfrequency (red curve) and effective charging energy $E_{C,m} = c_m^2 e^2/(2C_{\mathrm{eff}})$ (blue curve) as functions of the mode number m. The calculations are carried out for $x_J/l = 0$ and $\phi_0 = \pi$. Note that only modes that couple to the Josephson junction are included. In this case only every other mode is coupled.

vanish in the limit $M \to \infty$. However, the effective charging energy appears to scale as $\sim 1/m^\gamma$, where $\gamma > 1$. Note that there is a clear change in the scaling behavior around $m \approx 20$, after which the effective charging energy decreases faster than the inverse eigenfrequency, implying that $\gamma > 1$ in the limit $m \to \infty$. In the context of the exponent in Eq. (D1), this results in a scaling given by $\lambda_m \sim (1/m)^{1+\gamma}$. Should the assumption $\gamma > 1$ hold true, it implies that the renormalization coefficient converges to a nonzero value, consistent with the behavior observed in Fig. 7.

Similar arguments regarding the convergence of the renormalization effects, especially when considering a Josephson junction that is capacitively coupled to the end of a CPW, are discussed in Refs. [41,56,57]. These works demonstrated that the magnitude of the coupling between the qubit mode and the high-frequency modes exhibits a natural cutoff frequency. This cutoff is primarily dependent on the Josephson capacitance C_J as $M \to \infty$. We observed similar behavior in the mode-dependent effective charging energies of the unimon circuit. Specifically, in the inset of Fig. 7, a natural frequency cutoff is apparent around $M \approx 50$. Although not shown in the figure, this cutoff is influenced by the selected value of C_J.

APPENDIX E: ACCURACY OF THE MULTIMODE MODEL

In this Appendix, we address the accuracy of the multimode model [Eq. (13)] compared with the single-mode model [Eq. (9)] and auxiliary-mode model [Eq. (1)]. Figure 8 illustrates that significant discrepancies in the lowest-mode anharmonicity between the two models arise primarily at two flux bias points: $\Phi_{\mathrm{diff}}/\Phi_0 = 0.39$ and 0.50. We observe that if the number of auxiliary modes increases from $M = 2$ to $M = 4$, the anharmonicity undergoes corrections of approximately
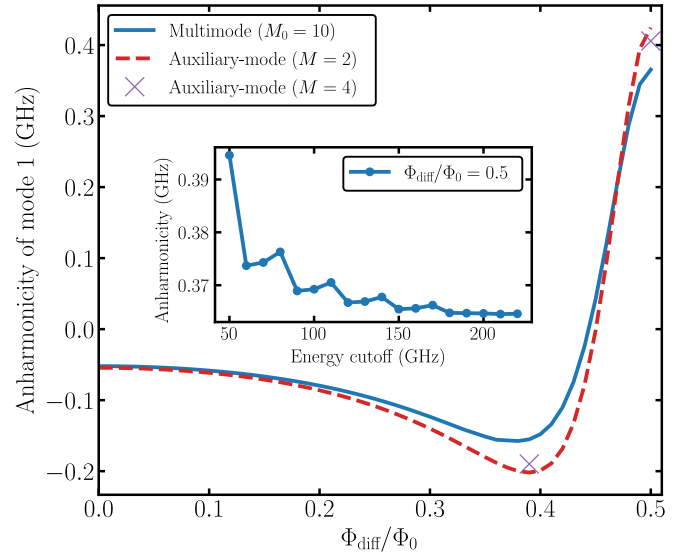

FIG. 8. Anharmonicity of the lowest mode as a function of the $\Phi_{\mathrm{diff}}/\Phi_0$ for the multimode ($M_0 = 10$) and auxiliary-mode ($M = 2$) models. In addition, two data points for the auxiliary-mode model with $M = 4$ are shown at positions where the deviation between the two models is most pronounced ($\Phi_{\mathrm{diff}}/\Phi_0 = 0.39$ and 0.50). The inset shows the anharmonicity of lowest mode as a function of the energy cutoff E_{cutoff}, as determined by the multimode model. The parameters used for these calculations are $x_J/l = 0$, $L_l = 0.83\,\mu\mathrm{H/m}$, $C_l = 83.0\,\mathrm{pF/m}$, and $E_J/h \approx 19.0\,\mathrm{GHz}$.

15 MHz in magnitude. In both instances, these corrections move the value closer to what is obtained with the multimode model. In addition, the inset of Fig. 8 reveals a convergent behavior for the multimode model, exhibiting markedly smaller deviations than the auxiliary-mode model as the energy cutoff E_{cutoff} surpasses 100 GHz. For instance, if E_{cutoff} is increased from 150 to 200 GHz, the correction to the anharmonicity is roughly 1 MHz.

We also performed a fitting procedure for the multimode model by using the measurement results from Ref. [27]. A good fit for the transition frequencies f_{01} and f_{02}, as function of Φ_{diff}, was found by using parameter values $L_l \approx 0.809\,\mu\mathrm{H/m}$, $C_l \approx 88.1\,\mathrm{pF/m}$, and $E_J/h \approx 21.2\,\mathrm{GHz}$. The fitting results of MMM, along with the other models, are depicted in Fig. 9, while the fitting parameters for each model are detailed in Table III.

The multimode model demonstrates a high degree of agreement with the experimental data, particularly at the sweet spots. Nonetheless, minor deviations from the measured transition frequencies are observed outside of these sweet spots across all models. As expected, the multimode model consistently outperforms the single-mode model, offering a universally superior fit. The fitting results reflect the renormalization of the Josephson energy, attributed to the zero-point fluctuations of the additional modes, resulting in an increase in the Josephson energy as predicted by the multimode model (refer to Table III). The renormalization coefficient, calculated as $\tilde{E}_J/E_J \approx 19.0/21.2 = 0.896$, aligns closely with theoretical predictions in Fig. 4(b).

Surprisingly, the auxiliary-mode model provides a better fit compared to the multimode model, which is especially
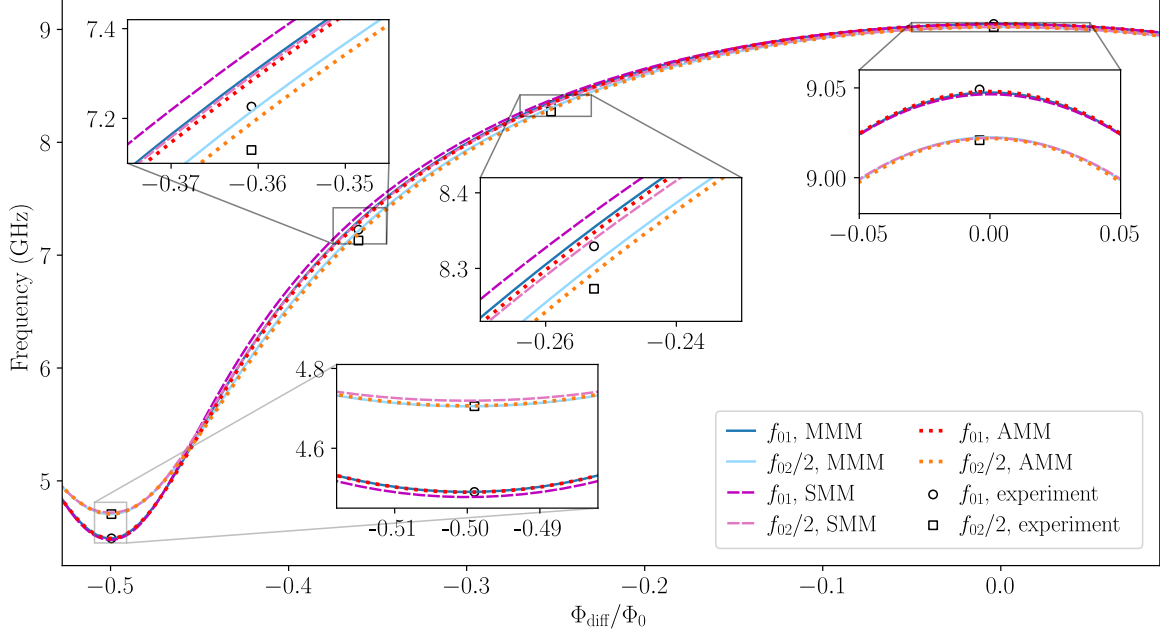
FIG. 9. Fitting results for the transition frequencies f_{01} and f_{02}, utilizing multimode model (MMM), single-mode model (SMM), and auxiliary-mode model (AMM), based on measurement results from Ref. [27]. Optimized fitting parameters for each model are detailed in Table III.

clear outside of the sweet spots. The observed discrepancy is modest, approximately 10 MHz for $f_{02}/2$ at $\Phi_{\text{diff}}/\Phi_0 = -0.36$, and could be partially attributed to the exclusion of the first excited levels for modes $m > M_0$. This omission is significant because the coupling strength between the ground state of the mode and its first excited level peaks away from the sweet spots, closely mirroring the behavior described by the function $|\sin(\varphi_0)|$. Supporting this explanation, the deviation between the two models also approximates the form of $|\sin(\varphi_0)|$, with both reaching the maximum value at $\Phi_{\text{diff}}/\Phi_0 \approx -0.38$. Although not implemented here, we anticipate that the Schrieffer-Wolff transformation could effectively approximate this effect.

APPENDIX F: DEPENDENCE OF THE UNIMON PHYSICS ON E_J AND Z_c

We investigate the interplay between the Josephson energy, E_J, and the characteristic impedance, Z_c, in a unimon operated at its sweet spot of $\varphi = \pi$. We aim to understand how changes in these parameters influence the behavior of the system.

TABLE III. Optimal fitting parameters (E_J, L_l, and C_l) for the multimode model (MMM), single-mode model (SMM), and auxiliary-mode model (AMM), determined by fitting the models using measurement results from Ref. [27].

	E_J/h (GHz)	L_l (µH/m)	C_l (pF/m)
MMM	21.2	0.810	88.1
SMM	19.0	0.821	87.1
AMM	19.4	0.832	86.4

Starting with the auxiliary-mode Hamiltonian given by Eq. (1), we define new rescaled flux operators as $\hat{\tilde{\Psi}} = \sqrt{C_{\text{eff}}}\hat{\Psi}$ and $\hat{\tilde{\chi}}_m = \sqrt{C_{\text{eff}}}\hat{\chi}_m$. The corresponding charge operators are defined as $\hat{\tilde{Q}} = \hat{Q}/\sqrt{C_{\text{eff}}}$ and $\hat{\tilde{\Xi}}_m = \hat{\Xi}_m/\sqrt{C_{\text{eff}}}$. This modification presents us with the Hamiltonian

$$\hat{H}_{\text{aux}} = \frac{\hat{\tilde{Q}}^2}{2} + \frac{\hat{\tilde{\Psi}}^2}{2L_{\text{eff}}C_{\text{eff}}} + E_J \cos\left(\frac{2\pi}{\Phi_0}\frac{\hat{\tilde{\Psi}}}{\sqrt{C_{\text{eff}}}}\right)$$
$$+ \sum_{m=1}^{M}\left[\frac{\hat{\tilde{\Xi}}_m^2}{2} + \frac{1}{2}\Omega_m^2\hat{\tilde{\chi}}_m^2 + \frac{\xi_m}{C_{\text{eff}}}\hat{\tilde{\chi}}_m\hat{\tilde{\Psi}}\right], \quad \text{(F1)}$$

where we have used effective inductance defined in Eq. (3). We assume that, given the high plasma frequency $\omega_p = 1/\sqrt{L_J C_J}$ compared to the frequencies of the primary normal modes, the Josephson capacitance C_J in the effective capacitance can be reasonably neglected. This assumption is reinforced by our numerical findings.

The characteristic impedance Z_c manifests in the relevant quantities as

$$C_{\text{eff}} \propto Z_c^{-1}, \quad L_{\text{eff}} \propto Z_c, \quad \xi_m \propto Z_c^{-1}. \quad \text{(F2)}$$

Applying these relations to Eq. (F1), it follows that the cosine term is the only one depending on Z_c. An expansion using a Taylor series provides

$$E_J \cos\left(\frac{\hat{\tilde{\varphi}}}{\sqrt{C_{\text{eff}}}}\right) = E_J - \beta_2 E_J Z_c \hat{\varphi}^2 + \beta_4 E_J Z_c^2 \hat{\varphi}^4 + \dots,$$

where β_2 and β_4 are constants, and $\hat{\tilde{\varphi}} = 2\pi\hat{\tilde{\Psi}}/\Phi_0$.

This expansion highlights an essential observation, that E_J and Z_c influence the system in roughly identical ways up to the second order. However, the distinction emerges in higher-order terms. Notably, the sensitivity of anharmonicity

to changes in Z_c increases with increasing Z_c. Yet, one must also account for the renormalization effects from other modes. These effects, which become more pronounced at greater Z_c, act to temper the increase in anharmonicity.

In summary, our investigation reveals that, within the bounds of our assumptions, an equal relative change in either E_J or Z_c produces an identical outcome on the system up to linear order. The differences primarily arise in high-order behavior and in the distinct effects of renormalization at an elevated Z_c.

APPENDIX G: ANALYTICAL CALCULATIONS IN THE HARMONIC-OSCILLATOR BASIS

We begin with examining the cosine term in the normal-mode representation, $E_J \cos(\sum_{m=1}^{M+1} \hat{\varphi}_m)$, which is the source of nonlinearity in our system. Following the steps taken in Ref. [34], we neglect the transverse-type interactions, rapidly rotating terms by the rotating-wave approximation, and Kerr-type interactions operating on more than three modes. This allows us to express the cosine term as

$$E_J \cos\left(\sum_{m=1}^{M+1} \hat{\varphi}_m\right) \approx E_J \prod_{m=1}^{M+1} e^{-\lambda_m^2/2}\left(1 - \lambda_m^2 \hat{a}_m^\dagger \hat{a}_m + \frac{\lambda_m^4}{4}\hat{a}_m^\dagger \hat{a}_m^\dagger \hat{a}_m \hat{a}_m + \dots\right)$$

$$\approx -E_J^* \sum_{m=1}^{M+1}\left(\lambda_m^2 \hat{a}_m^\dagger \hat{a}_m - \frac{\lambda_m^4}{4}\hat{a}_m^\dagger \hat{a}_m^\dagger \hat{a}_m \hat{a}_m + \dots\right)\left[1 - \sum_{\substack{n=1 \\ n\neq m}}^{M+1} \lambda_n^2 \hat{a}_n^\dagger \hat{a}_n + \frac{1}{2}\sum_{\substack{k=1 \\ k\neq m}}^{M+1} \lambda_k^2 \hat{a}_k^\dagger \hat{a}_k \sum_{\substack{l=1 \\ l\notin\{m,k\}}}^{M+1} \lambda_l^2 \hat{a}_l^\dagger \hat{a}_l\right], \quad \text{(G1)}$$

where we have used the harmonic-oscillator basis $\hat{\varphi}_m = \lambda_m(\hat{a}_m^\dagger + \hat{a}_m)$ and $E_J^* = E_J \prod_{m=1}^{M+1} e^{-\lambda_m^2/2}$. From this result, we identify the self- and cross-Kerr interactions including high-order corrections for any three-mode combination as given in Eqs. (19) and (20) of the main text.

[1] J. M. Gambetta, J. M. Chow, and M. Steffen, Building logical qubits in a superconducting quantum computing system, npj Quantum Inf. **3**, 2 (2017).

[2] J. Koch, T. M. Yu, J. Gambetta, A. A. Houck, D. I. Schuster, J. Majer, A. Blais, M. H. Devoret, S. M. Girvin, and R. J. Schoelkopf, Charge-insensitive qubit design derived from the Cooper pair box, Phys. Rev. A **76**, 042319 (2007).

[3] A. P. M. Place, L. V. H. Rodgers, P. Mundada, B. M. Smitham, M. Fitzpatrick, Z. Leng, A. Premkumar, J. Bryon, A. Vrajitoarea, S. Sussman, G. Cheng, T. Madhavan, H. K. Babla, X. H. Le, Y. Gang, B. Jäck, A. Gyenis, N. Yao, R. J. Cava, N. P. de Leon, and A. A. Houck, New material platform for superconducting transmon qubits with coherence times exceeding 0.3 milliseconds, Nat. Commun. **12**, 1779 (2021).

[4] C. Wang, X. Li, H. Xu, Z. Li, J. Wang, Z. Yang, Z. Mi, X. Liang, T. Su, C. Yang, G. Wang, W. Wang, Y. Li, M. Chen, C. Li, K. Linghu, J. Han, Y. Zhang, Y. Feng, Y. Song, T. Ma, J. Zhang, R. Wang, P. Zhao, W. Liu, G. Xue, Y. Jin, and H. Yu, Transmon qubit with relaxation time exceeding 0.5 milliseconds, npj Quantum Inf. **8**, 3 (2022).

[5] J. Preskill, Quantum computing in the NISQ era and beyond, Quantum **2**, 79 (2018).

[6] V. E. Manucharyan, J. Koch, L. I. Glazman, and M. H. Devoret, Fluxonium: Single cooper-pair circuit free of charge offsets, Science **326**, 113 (2009).

[7] J. Koch, V. Manucharyan, M. H. Devoret, and L. I. Glazman, Charging effects in the inductively shunted Josephson junction, Phys. Rev. Lett. **103**, 217004 (2009).

[8] F. Bao, H. Deng, D. Ding, R. Gao, X. Gao, C. Huang, X. Jiang, H.-S. Ku, Z. Li, X. Ma, X. Ni, J. Qin, Z. Song, H. Sun, C. Tang, T. Wang, F. Wu, T. Xia, W. Yu, F. Zhang, G. Zhang, X. Zhang, J. Zhou, X. Zhu, Y. Shi, J. Chen, H.-H.

Zhao, and C. Deng, Fluxonium: An alternative qubit platform for high-fidelity operations, Phys. Rev. Lett. **129**, 010502 (2022).

[9] H. Zhang, S. Chakram, T. Roy, N. Earnest, Y. Lu, Z. Huang, D. K. Weiss, J. Koch, and D. I. Schuster, Universal fast-flux control of a coherent, low-frequency qubit, Phys. Rev. X **11**, 011010 (2021).

[10] A. Somoroff, Q. Ficheux, R. A. Mencia, H. Xiong, R. Kuzmin, and V. E. Manucharyan, Millisecond coherence in a superconducting qubit, Phys. Rev. Lett. **130**, 267001 (2023).

[11] L. Ding, M. Hays, Y. Sung, B. Kannan, J. An, A. Di Paolo, A. H. Karamlou, T. M. Hazard, K. Azar, D. K. Kim, B. M. Niedzielski, A. Melville, M. E. Schwartz, J. L. Yoder, T. P. Orlando, S. Gustavsson, J. A. Grover, K. Serniak, and W. D. Oliver, High-fidelity, frequency-flexible two-qubit fluxonium gates with a transmon coupler, Phys. Rev. X **13**, 031035 (2023).

[12] L. B. Nguyen, G. Koolstra, Y. Kim, A. Morvan, T. Chistolini, S. Singh, K. N. Nesterov, C. Jünger, L. Chen, Z. Pedramrazi, B. K. Mitchell, J. M. Kreikebaum, S. Puri, D. I. Santiago, and I. Siddiqi, Blueprint for a high-performance fluxonium quantum processor, PRX Quantum **3**, 037001 (2022).

[13] L. B. Nguyen, Y.-H. Lin, A. Somoroff, R. Mencia, N. Grabon, and V. E. Manucharyan, High-coherence fluxonium qubit, Phys. Rev. X **9**, 041041 (2019).

[14] T. M. Hazard, A. Gyenis, A. Di Paolo, A. T. Asfaw, S. A. Lyon, A. Blais, and A. A. Houck, Nanowire superinductance fluxonium qubit, Phys. Rev. Lett. **122**, 010504 (2019).

[15] M. Peruzzo, F. Hassani, G. Szep, A. Trioni, E. Redchenko, M. Žemlička, and J. M. Fink, Geometric superinductance qubits: controlling phase delocalization across a single Josephson junction, PRX Quantum **2**, 040341 (2021).

[16] F. Yan, Y. Sung, P. Krantz, A. Kamal, D. K. Kim, J. L. Yoder, T. P. Orlando, S. Gustavsson, and W. D. Oliver, Engineering framework for optimizing superconducting qubit designs, arXiv:2006.04130.

[17] Y. Ye, K. Peng, M. Naghiloo, G. Cunningham, and K. P. O'Brien, Engineering purely nonlinear coupling between superconducting qubits using a quarton, Phys. Rev. Lett. **127**, 050502 (2021).

[18] A. B. Zorin and F. Chiarello, Superconducting phase qubit based on the Josephson oscillator with strong anharmonicity, Phys. Rev. B **80**, 214535 (2009).

[19] F.-M. Liu, C. Wang, M.-C. Chen, H. Chen, S.-W. Li, Z.-X. Shang, C. Ying, J.-W. Wang, Y.-H. Huo, C.-Z. Peng, X. Zhu, C.-Y. Lu, and J.-W. Pan, Quantum computer-aided design for advanced superconducting qubit: Plasmonium, Sci. Bull. **68**, 1625 (2023).

[20] I. V. Pechenezhskiy, R. A. Mencia, L. B. Nguyen, Y.-H. Lin, and V. E. Manucharyan, The superconducting quasicharge qubit, Nature (London) **585**, 368 (2020).

[21] L. Chirolli, M. Carrega, and F. Giazotto, The quartic Blochnium: an anharmonic quasicharge superconducting qubit, Quantum **7**, 1193 (2023).

[22] A. Gyenis, P. S. Mundada, A. Di Paolo, T. M. Hazard, X. You, D. I. Schuster, J. Koch, A. Blais, and A. A. Houck, Experimental realization of a protected superconducting circuit derived from the $0 - \pi$ qubit, PRX Quantum **2**, 010339 (2021).

[23] K. Kalashnikov, W. T. Hsieh, W. Zhang, W.-S. Lu, P. Kamenov, A. Di Paolo, A. Blais, M. E. Gershenson, and M. Bell, Bifluxon: Fluxon-parity-protected superconducting qubit, PRX Quantum **1**, 010307 (2020).

[24] W. C. Smith, A. Kou, X. Xiao, U. Vool, and M. H. Devoret, Superconducting circuit protected by two-Cooper-pair tunneling, npj Quantum Inf. **6**, 8 (2020).

[25] S. Richer, N. Maleeva, S. T. Skacel, I. M. Pop, and D. DiVincenzo, Inductively shunted transmon qubit with tunable transverse and longitudinal coupling, Phys. Rev. B **96**, 174520 (2017).

[26] F. Hassani, M. Peruzzo, L. N. Kapoor, A. Trioni, M. Zemlicka, and J. M. Fink, Inductively shunted transmons exhibit noise insensitive plasmon states and a fluxon decay exceeding 3 hours, Nat. Commun. **14**, 3968 (2023).

[27] E. Hyyppä, S. Kundu, C. F. Chan, A. Gunyhó, J. Hotari, D. Janzso, K. Juliusson, O. Kiuru, J. Kotilahti, A. Landra, W. Liu, F. Marxer, A. Mäkinen, J.-L. Orgiazzi, M. Palma, M. Savytskyi, F. Tosto, J. Tuorila, V. Vadimov, T. Li, C. Ockeloen-Korppi, J. Heinsoo, K. Y. Tan, J. Hassel, and M. Möttönen, Unimon qubit, Nat. Commun. **13**, 6895 (2022).

[28] The voltage profiles follow the definitions of the mode envelope functions $u_m(x)$ which were derived in the supplemental material of Ref. [27]. Note that here the voltage profiles serve primarily as a visual aid. They illustrate the coupling of multiple modes to the Josephson junction, thereby demonstrating their interconnectivity

[29] S. E. Nigg, H. Paik, B. Vlastakis, G. Kirchmair, S. Shankar, L. Frunzio, M. H. Devoret, R. J. Schoelkopf, and S. M. Girvin, Black-box superconducting circuit quantization, Phys. Rev. Lett. **108**, 240502 (2012).

[30] F. Solgun, D. W. Abraham, and D. P. DiVincenzo, Blackbox quantization of superconducting circuits using exact impedance synthesis, Phys. Rev. B **90**, 134504 (2014).

[31] J. Bourassa, F. Beaudoin, J. M. Gambetta, and A. Blais, Josephson-junction-embedded transmission-line resonators: From Kerr medium to in-line transmon, Phys. Rev. A **86**, 013814 (2012).

[32] H. L. Mortensen, K. Mølmer, and C. K. Andersen, Normal modes of a superconducting transmission-line resonator with embedded lumped element circuit components, Phys. Rev. A **94**, 053817 (2016).

[33] W. C. Smith, A. Kou, U. Vool, I. M. Pop, L. Frunzio, R. J. Schoelkopf, and M. H. Devoret, Quantization of inductively shunted superconducting circuits, Phys. Rev. B **94**, 144507 (2016).

[34] M. Leib, F. Deppe, A. Marx, R. Gross, and M. J. Hartmann, Networks of nonlinear superconducting transmission line resonators, New J. Phys. **14**, 075024 (2012).

[35] S. Léger, J. Puertas-Martínez, K. Bharadwaj, R. Dassonneville, J. Delaforce, F. Foroughi, V. Milchakov, L. Planat, O. Buisson, C. Naud, W. Hasch-Guichard, S. Florens, I. Snyman, and N. Roch, Observation of quantum many-body effects due to zero point fluctuations in superconducting circuits, Nat. Commun. **10**, 5259 (2019).

[36] A. J. Kerman, Efficient numerical simulation of complex Josephson quantum circuits, arXiv:2010.14929.

[37] T. Roy, M. Chand, A. Bhattacharjee, S. Hazra, S. Kundu, K. Damle, and R. Vijay, Multimode superconducting circuits for realizing strongly coupled multiqubit processor units, Phys. Rev. A **98**, 052318 (2018).

[38] T. Roy, S. Hazra, S. Kundu, M. Chand, M. P. Patankar, and R. Vijay, Programmable superconducting processor with native three-qubit gates, Phys. Rev. Appl. **14**, 014072 (2020).

[39] T. Roy, S. Kundu, M. Chand, S. Hazra, N. Nehra, R. Cosmic, A. Ranadive, M. P. Patankar, K. Damle, and R. Vijay, Implementation of pairwise longitudinal coupling in a three-qubit superconducting circuit, Phys. Rev. Appl. **7**, 054025 (2017).

[40] Properties of the eigenstates in the low-energy subspace seem to be relatively insensitive to changes in C_J when typical values are used ($C_J \sim 1$ fF). This is not surprising since the value in question is much smaller than the full capacitance of the CPW resonator ($2lC_l \sim 500$ fF).

[41] M. F. Gely, A. Parra-Rodriguez, D. Bothner, Y. M. Blanter, S. J. Bosman, E. Solano, and G. A. Steele, Convergence of the multimode quantum Rabi model of circuit quantum electrodynamics, Phys. Rev. B **95**, 245115 (2017).

[42] S. Filipp, M. Göppl, J. M. Fink, M. Baur, R. Bianchetti, L. Steffen, and A. Wallraff, Multimode mediated qubit-qubit coupling and dark-state symmetries in circuit quantum electrodynamics, Phys. Rev. A **83**, 063827 (2011).

[43] A. Frisk Kockum, P. Delsing, and G. Johansson, Designing frequency-dependent relaxation rates and Lamb shifts for a giant artificial atom, Phys. Rev. A **90**, 013837 (2014).

[44] D. G. Ferguson, A. A. Houck, and J. Koch, Symmetries and collective excitations in large superconducting circuits, Phys. Rev. X **3**, 011003 (2013).

[45] A. Gyenis, A. Di Paolo, J. Koch, A. Blais, A. A. Houck, and D. I. Schuster, Moving beyond the transmon: Noise-protected

superconducting quantum circuits, PRX Quantum **2**, 030101 (2021).

[46] A. Kitaev, Protected qubit based on a superconducting current mirror, arXiv:cond-mat/0609441.

[47] D. K. Weiss, A. C. Y. Li, D. G. Ferguson, and J. Koch, Spectrum and coherence properties of the current-mirror qubit, Phys. Rev. B **100**, 224507 (2019).

[48] A detailed derivation of the Lagrangian is provided in the Supplemental Material of Ref. [27].

[49] H. Goldstein, J. Safko, and C. Poole, *Classical Mechanics: Pearson New International Edition* (Pearson Education, Harlow, Essex, 2014).

[50] J. Defrance and T. Weiss, On the pole expansion of electromagnetic fields, Opt. Express **28**, 32363 (2020).

[51] G. B. Arfken, H. J. Weber, and F. E. Harris, *Mathematical Methods for Physicists* (Academic Press, Boston, 2013), pp. 515–516.

[52] M. K. Zinn, Network representation of transcendental impedance functions, Bell Syst. Tech. J. **31**, 378 (1952).

[53] A. Miano, V. R. Joshi, G. Liu, W. Dai, P. D. Parakh, L. Frunzio, and M. H. Devoret, Hamiltonian extrema of an arbitrary flux-biased Josephson circuit, PRX Quantum **4**, 030324 (2023).

[54] M. Rymarz and D. P. DiVincenzo, Consistent quantization of nearly singular superconducting circuits, Phys. Rev. X **13**, 021017 (2023).

[55] D. K. Weiss, W. DeGottardi, J. Koch, and D. G. Ferguson, Variational tight-binding method for simulating large superconducting circuits, Phys. Rev. Res. **3**, 033244 (2021).

[56] A. Parra-Rodriguez, E. Rico, E. Solano, and I. L. Egusquiza, Quantum networks in divergence-free circuit QED, Quantum Sci. Technol. **3**, 024012 (2018).

[57] M. Malekakhlagh, A. Petrescu, and H. E. Türeci, Cutoff-free circuit quantum electrodynamics, Phys. Rev. Lett. **119**, 073601 (2017).